Key Points:
- A simple biogeochemistry module is described to simulate ocean phosphorus, iron, oxygen, organic and inorganic carbon, and alkalinity cycles
- This module has been run in a new climate model with quarter degree resolution ocean and compares well with observations
- This steady-state ecosystem provides a computationally light means to simulate large-scale patterns in ocean biogeochemical tracers

Supporting Information:
- Supporting Information S1

Correspondence to:
J. P. Dunne,
john.dunne@noaa.gov

Simple Global Ocean Biogeochemistry With Light, Iron, Nutrients and Gas Version 2 (BLINGv2): Model Description and Simulation Characteristics in GFDL's CM4.0

J. P. Dunne[1] [ID], **I. Bociu[2]**, **B. Bronselaer[3]**, **H. Guo[4,1]** [ID], **J. G. John[1]** [ID], **J. P. Krasting[1]** [ID], **C. A. Stock[1]** [ID], **M. Winton[1]** [ID], and **N. Zadeh[5]** [ID]

[1]NOAA/OAR Geophysical Fluid Dynamics Laboratory, Princeton, NJ, USA, [2]Cooperative Institute for Modeling the Earth System, Princeton University, Princeton, NJ, USA, [3]Department of Geosciences, University of Arizona, Tucson, AZ, USA, [4]UCAR/GFDL, Princeton, NJ, USA, [5]SAIC/GFDL, Princeton, NJ, USA

Abstract Simulation of coupled carbon-climate requires representation of ocean carbon cycling, but the computational burden of simulating the dozens of prognostic tracers in state-of-the-art biogeochemistry ecosystem models can be prohibitive. We describe a six-tracer biogeochemistry module of steady-state phytoplankton and zooplankton dynamics in Biogeochemistry with Light, Iron, Nutrients and Gas (BLING version 2) with particular emphasis on enhancements relative to the previous version and evaluate its implementation in Geophysical Fluid Dynamics Laboratory's (GFDL) fourth-generation climate model (CM4.0) with ¼° ocean. Major geographical and vertical patterns in chlorophyll, phosphorus, alkalinity, inorganic and organic carbon, and oxygen are well represented. Major biases in BLINGv2 include overly intensified production in high-productivity regions at the expense of productivity in the oligotrophic oceans, overly zonal structure in tropical phosphorus, and intensified hypoxia in the eastern ocean basins as is typical in climate models. Overall, while BLINGv2 structural limitations prevent sophisticated application to plankton physiology, ecology, or biodiversity, its ability to represent major organic, inorganic, and solubility pumps makes it suitable for many coupled carbon-climate and biogeochemistry studies including eddy interactions in the ocean interior. We further overview the biogeochemistry and circulation mechanisms that shape carbon uptake over the historical period. As an initial analysis of model historical and idealized response, we show that CM4.0 takes up slightly more anthropogenic carbon than previous models in part due to enhanced ventilation in the absence of an eddy parameterization. The CM4.0 biogeochemistry response to CO_2 doubling highlights a mix of large declines and moderate increases consistent with previous models.

Plain Language Summary Cutting edge climate model development efforts often do not include representation of the carbon cycle and biogeochemical tracers due to the large computational expense of these additional tracers. During GFDL CM4.0 development, an effort was made to include a simple representation of these processes to explore ocean biogeochemistry at eddying resolution. This simple ocean biogeochemistry builds on the previous BLINGv1 effort (Galbraith et al., 2010, https://doi.org/10.5194/bg-7-1043-2010) and is suitable for carbon uptake and provides a computationally light means to simulate large-scale patterns in ocean biogeochemical tracers.

1. Introduction

Simple representations of ocean biogeochemical cycles are an important tool for understanding a variety of processes including the biological, solubility and calcium carbonate pumps, and co-limitation of biological productivity. They are also highly advantageous for elucidating ocean circulation pathways along which remineralization accumulates in the ocean interior and the sensitivity of large-scale biogeochemical processes to circulation and biogeochemical forcing variability and change. Critical among these are the environmental change questions of ocean anthropogenic carbon uptake (Frölicher et al., 2015), acidification (Doney et al., 2009), productivity change (Bopp et al., 2013), and hypoxia (e.g., Oschlies et al., 2008). The earliest of these was the Hamburg Model of the Ocean Carbon Cycle (HAMOCC) (Bacastow & Maier-Reimer, 1990; Maier-Reimer, 1993) used for early characterization of the various ocean carbon pumps.

These ideas grew into a fully prognostic, yet still highly simplified, representation of ocean ecosystems used for climate change studies in Bopp et al. (2001). Archer and Johnson (2000), using a three-dimensional, global circulation and biogeochemistry model, examine three parameterizations of iron cycling. Two early prognostic models to represent co-limitation were the multiple plankton group model of Dutkiewicz et al. (2005) with co-limitation of iron and phosphate and phytoplankton functional diversity model of Le Quere et al. (2005). Another was the simple ocean biogeochemistry used for long time scale fully coupled carbon-climate Earth system model experiments (Doney et al., 2006).

Meanwhile, ever-increasing complexity models showcasing phytoplankton functional diversity contributed to the various model intercomparison efforts over the last decade (e.g., Bopp et al., 2013; Friedlingstein et al., 2006). These biogeochemical modules typically double to quadruple the computational cost of running ocean simulations and thus are difficult to rationalize in climate-focused studies. In their effort to address this, Galbraith et al. (2010, 2015) developed the Biogeochemistry with Light, Iron, Nutrients and Gas (BLINGv1) module which allowed exploration of carbon cycle and co-limitation questions with less than doubling of the computational cost of the model. Like previous efforts, it chose to focus on representation of the phosphorus over nitrogen as master nutrient in the role of phosphorus as ultimate nutrient (Toggweiler, 1999; Tyrrell, 1999) and to promote analysis of apparent oxygen utilization (Redfield et al., 1963) in the ocean interior which would be confounded with nitrogen as master nutrient due to complications under fixation and denitrification. The distinction of BLINGv1 among previous simple biogeochemical models was that it was built with ecological formulations for phytoplankton biomass, chlorophyll, size structure, and particle export efficiency for distinguishing new versus regenerated production. These improved the mechanistic underpinnings of the model (subject to the aforementioned computational constraints) and allowed it to be compared directly with a suite of observational metrics of ecosystem states processes.

The present study builds on previous BLINGv1 work to improve the mechanistic representation of important ecological and biogeochemical processes taking advantage of more advanced mechanisms in TOPAZv2 (Dunne et al., 2013) and COBALT (Stock & Dunne, 2010; Stock et al., 2014a, 2014b) and to improve comparability to observations. This BLINGv2 model is applied within Geophysical Fluid Dynamics Laboratory's (GFDL) new CM4.0 (Held et al., 2019) model with the 1° horizontal and 33 hybrid layer vertical resolution "fast chemistry" AM4.0 atmosphere (Zhao et al., 2018) and ¼° horizontal and 75 hybrid layer vertical resolution OM4 ocean using Modular Ocean Model version 6 (MOM6; Adcroft et al., 2019). GFDL's fully comprehensive coupled carbon-chemistry-climate Earth system model, ESM 4.1, that includes state-of-the-art ocean biogeochemistry based on COBALTv2 (Stock et al., 2020) is described elsewhere (Dunne et al., 2020).

BLINGv2 was developed with the intention of having sufficient comprehensiveness, numerical efficiency, and fidelity to allow CM4.0 to participate to intercomparisons of projection scenarios (ScenarioMIP; O'Neill et al., 2016), the coupled climate-carbon cycle (C4MIP; Jones et al., 2016), and ocean biogeochemistry (OMIP-BGC; Orr et al., 2017). Simulations include an 1850 control, 1%, and historical configurations that are part of the sixth phase of the Coupled Model Intercomparison Project (CMIP6; Eyring et al., 2016). We describe the BLINGv2 formulation paying particular attention to improvements in the biogeochemistry scheme relative to the previous BLINGv1 (Galbraith et al., 2010) before describing the model's baseline fidelity and response to historical and idealized forcing. As one of the primary intended applications of BLINGv2 is the representation of ocean carbon system response to increasing atmospheric CO_2 and the associated ocean acidification, we explore those mechanisms.

2. Model Description

The first-generation module for BLING was developed by Galbraith et al. (2010) with explicit representation of dissolved inorganic carbon (DIC), alkalinity, phosphate, dissolved iron, dissolved organic phosphorus (DOP), and O_2 pools implemented in Modular Ocean Model version 4.1 (MOM4p1) (Griffies et al., 2005). Instead of representing phytoplankton, zooplankton, and other ecosystem structure and function through explicit, prognostic tracers, BLINGv2 includes an implicit physiological model of growth co-limitation by light, temperature, phosphate, and iron and an implicit ecological model of partitioning into remineralized and dissolved pools after Dunne et al. (2005). The present version (BLINGv2) maintains this basic biogeochemical structure shown as schematic in Figure 1 to sole equations of state for dissolved inorganic
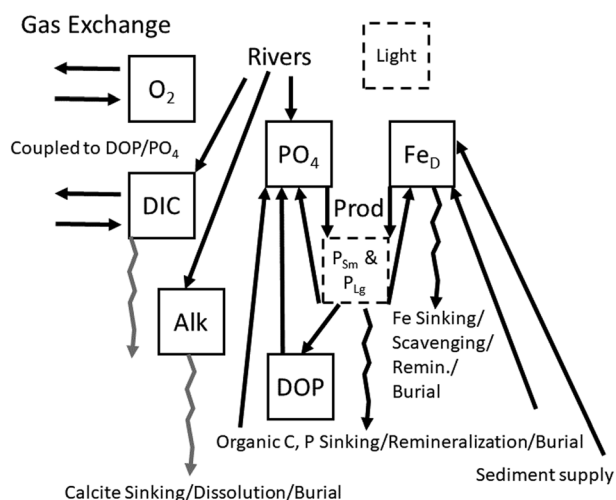
Figure 1. Model schematic of BLINGv2 where solid boxes represent explicit tracers and dashed box represents steady-state calculations of physiological state and ecosystem function after Dunne et al. (2005). Solid boxes represent the explicit prognostic evolution of the equations of state for dissolved inorganic phosphate (PO_4), dissolved inorganic carbon (DIC), dissolved organic phosphorus (DOP), alkalinity (Alk), oxygen (O_2), and dissolved iron (Fe_D). Dashed boxes represent ecosystem components for small and large phytoplankton, zooplankton, and detritus set to steady state and light forcing as diagnostic tracers. Black arrows are provided for phosphorus and iron fluxes through production and remineralization. Gray arrows are provided for calcite cycling. The equivalent arrows for organic matter cycling impacts on DIC, O_2, and Alk are omitted for clarity in presentation.

phosphate (PO_4), DIC, DOP, alkalinity (Alk), oxygen (O_2), and dissolved iron (Fe_D). BLINGv2 takes advantage of improvements in ocean numerics with MOM6 (Adroft et al., 2019) and improved representation of phytoplankton physiology, food web processing in the euphotic zone and remineralization/dissolution through the ocean interior, and elemental coupling that have been since incorporated into GFDL's more recent and more sophisticated TOPAZv2 (Dunne et al., 2013) and later COBALT (Stock et al., 2014a) model development efforts to address some of the weaknesses in the original BLING. The following subsections provide highlights of the BLINGv2 algorithms. A full technical description of all BLINGv2 equations and parameter values is provided as supporting information.

2.1. Numerics

A detailed description of MOM6 numerics implemented in the ocean component of CM4 is provided in Adcroft et al. (2019). Highlights include a horizontal resolution of ¼° with 75 hyrid z* and isopycnal layers with 2-m resolution in the upper ocean with the three-dimensional arbitrary Lagrangian-Eulerian method of Hirt et al. (1997) for time stepping and the third-order piecewise parabolic method of Huynh (1995) for tracer advection. The ice-ocean system exhibits dynamically coupled modes that should be well resolved numerically and integrated forward consistently. In previous GFDL coupled models, several modes of numerical instability associated with atmosphere-ice-ocean interactions forced coupling time steps and associated ocean tracer time steps to be reduced far below the limit set by tracer advection and other interior ocean factors. Two major numerical achievements in the MOM6 effort relating to tracer applications were combining the splitting of dynamical and tracer time steps within the ocean as was done in ESM2G (Dunne et al., 2013) with an innovative ability to have tracer time steps span the atmosphere-ice-ocean coupling time step. The ice and ocean models are integrated forward in time independently and coupled using the forward Euler method which is conditionally stable dependent on the ice thickness, the ocean vertical resolution, and the coupling frequency which limits the range of stable time steps (Hallberg, 2014). Together, these improvements allow ocean tracers to be run with a tracer time step of 2 h even though the dynamical time step is 15 min and coupling with the sea ice and atmosphere is every 30 min to assure coupled model stability. Thus, the six-tracer BLINGv2 consumes only an additional 15% of computing over the physical ocean model alone to greatly improve the practical potential of its widespread use in climate models to diagnose ocean biogeochemical variability and change.

2.2. Phytoplankton Growth

Photosynthesis is formulated in general as in Geider et al. (1997). This formulation gives a biomass-specific growth rate as a function of light, nutrient limitation, and temperature in a physiological steady state. We modify this relationship slightly and also use the assumption of steady-state growth versus loss to derive a simple relationship between growth rate, biomass, and uptake. The instantaneous irradiance field is modulated in its impact on the C:Chl ratio by being averaged throughout the mixed layer plus one more vertical layer to account for mixing directly below the boundary layer. This quantity is intended to represent the light to which phytoplankton subject to turbulent transport in the mixed layer would be exposed. This irradiance memory is a temporally smoothed field carried between time steps, to represent photoadaptation with the Chl:C response rate constant for phytoplankton calibrated to 1 d^{-1} after Owens et al. (1980). Temperature functionality of growth and grazing is represented by the equation of Eppley (1972) for both simplicity and to incorporate combined effects on uptake, incorporation into organic matter, and photorespiration. Values of maximum potential growth rates are normalized to 0°C rather than 20°C in Geider et al. (1997).

Limitation terms for PO_4 and Fe_D and the iron-limited Chl:C maximum are calculated via the Monod (1949) equation to estimate productivity and update biomass as described in the supporting information with values set to match equatorial Pacific growth rate observations (Landry et al., 1997). The iron deficiency

follows a sigmoidal functional form with chlorosis factor to conform to the observations of Sunda and Huntsman (1997). The light-saturated maximal photosynthesis rate term is the product of a prescribed maximum photosynthesis rate, the Eppley (1972) temperature dependence, and a Liebig limitation (the minimum of Michaelis-Menton PO_4 limitation or iron limitation with the maximum growth rate constant set to be consistent with Bissinger et al., 2008, of 0.82 d^{-1} at 0°C). Calculation of the maximum allowed chlorophyll-to-carbon ratio and slope of the photosynthesis-irradiance curve are based on the iron deficiency but with a minimum offset to represent the ability of phytoplankton to use other trace metals. The highest allowed chlorophyll-to-carbon ratio and initial slope and minimum values were set to match the TOPAZv2 value for small phytoplankton. These changes served to decrease surface chlorophyll and deepen the euphotic zone to better agree with observations. These values are then used to calculate the irradiance limitation based on the memory of irradiance with a 1-day filter and overall growth rate based on the instantaneous irradiance but averaged within the mixed layer. The nutrient-limited efficiency of algal photosystems is calculated. The iron deficiency term is included here as a multiplier of the maximum Chl:C ratio to represent the importance of Fe in forming chlorophyll accessory antennae, which do not affect the Chl:C but still affect the phytoplankton ability to use light (Strzepek & Harrison, 2004). This is prescribed as a fraction of the light-saturated photosynthesis rate. The result is a set level of energy availability below which net growth (and therefore nutrient uptake) is zero. We also calculate the Chl:C ratio for the diagnostic chlorophyll concentration. The carbon-specific photosynthesis rate accounts for the maintenance effort that phytoplankton must exert to combat decay.

2.3. Ecosystem Functioning

The uptake of nutrients is assumed to contribute to the growth of phytoplankton which are consumed by heterotrophs within the same time step. This can involve the transfer of nutrient elements between many organic pools, both particulate and dissolved, with complex histories. BLINGv2 partitions the total uptake into two fractions—sinking and non-sinking—as a function of temperature following Dunne et al. (2005). Then, the non-sinking fraction is further subdivided, such that the majority is recycled instantaneously to the inorganic nutrient pool, representing the fast turnover of labile dissolved organic matter via the microbial loop, and 4% is converted to semi-labile dissolved organic matter that decays with a time scale of 18 years set to represent observed surface surplus and broad meridional and depth patterns in subtropical gyres based on Abell et al. (2000) and Hansell et al. (2009). Stoichiometric ratios for $CO_2:PO_4:O_2$ of 106:1:150 were taken from Anderson (1995). O_2 is handled the same as in BLINGv1. It should be noted that as in BLINGv1, BLINGv2 allows negative O_2 to represent the net oxidative deficit. While this decision was intended to make the model more consistent with the more complex models (e.g., Stock et al., 2020) and is arguably appropriate for representation of sulfate and iron reduction that consume O_2 and reoxidize when they come into oxic conditions, it ignores the important role of denitrification and should probably be removed in future versions. Iron and phosphorus are treated identically for the first step, but all iron is recycled instantaneously in the second step (i.e., there is no dissolved organic iron pool).

The original BLINGv1 calculated the fraction of phytoplankton that is large (>5 μm; frac$_{Lg}$) instantaneously at every depth. This led to unrealistic implied ecosystem changes both as a function of depth and over the diurnal cycle. To estimate phytoplankton structure, BLINGv2 makes use of the biomass-based phytoplankton size structure estimation method of Dunne et al. (2005), calculating a diagnostic biomass from the local uptake rate averaged over the mixed layer through the application of a simple phytoplankton biomass-based grazing formulation. Consistent with Dunne et al. (2005), calculation of the fraction of production by large phytoplankton and the associated conversion factors for phytoplankton losses into sinking particulate organic material is estimated as a single surface ocean euphotic zone estimate of current biomass, productivity, and particle export from the temporally and 100-m averaged previous biomass. Ecosystem state and associated fluxes are calculated from the evolving biomass by solving the cubic equation from Dunne et al. (2005; see supporting information for details). This biomass-based formulation provides a temporal and spatial ecosystem memory improvement over the instantaneous primary production calculation used in BLINGv1. The BLINGv2 calculation is motivated in part by the tendency for ecosystem "mixing" that while phytoplankton are primarily passive tracers as "plankton," zooplankton are able to move through the water column and take advantage of accumulations of prey such that the ecosystem comes to equilibrium with an "average" phytoplankton field. This parameterization helps damp the unrealistic vertical structure of uptake which

would obtain a biomass allowed to be at instantaneous equilibrium with the local growth rate constant. Calculation of biomass in BLINGv2 was also amended to respond on a 5-day rather than the 2-day time scale used in BLINGv1 to reduce high-frequency variability consistent with the growth rate of zooplankton biomass and associated limitations on the impact on phytoplankton (Landry & Hassett, 1982). The remainder is divided between instantaneously recycled (96%) and long-lived dissolved organic matter (4%).

2.4. Calcium Carbonate Cycling

Alkalinity is consumed through the production of $CaCO_3$ and is represented by a linear function of the implied growth rate of small phytoplankton that agrees with the global observational synthesis of $CaCO_3$ production and burial of Dunne et al. (2012). This representation is also consistent with the findings of Jin et al. (2006). Global $CaCO_3$ production was set to roughly match the observational synthesis of Dunne et al. (2012) of 0.56 PgC yr^{-1}. The $CaCO_3$ dissolution length scale is a function of the saturation state, CO_3 concentration divided by CO_3 solubility, such that the length scale decreases from infinity when the CO_3 concentration is greater than CO_3 solubility to 1,343 m at $CO_3 = 0$ calibrated to Station PAPA results as in TOPAZv2 (Dunne et al., 2013).

2.5. Remineralization

Rather than using a remineralization length scale that increases linearly with depth as in BLINGv1, BLINGv2 considers the simultaneous roles of bacterial colonization, oxygen (O_2), temperature, particle transformation and mineral protection on the remineralization length scale. A depth scale of 100 m is assumed for colonization of bacteria for remineralization of sinking material suppresses remineralization after Mislan et al. (2014) and Laufkötter et al. (2017). The $CaCO_3$ flux and a globally constant lithogenic flux are used in the mineral protection of sinking organic material of Klaas and Archer (2002) as in TOPAZ and COBALT. Unlike TOPAZ and COBALT, however, silicon cycling is ignored in BLINGv2. Relative to BLINGv1, this was found to reduce a spurious nutricline peak in remineralization and improve comparison of benthic organic carbon fluxes with observations. To represent the role of particle transformation, the remineralization length scale of unprotected detritus in BLINGv2 uses a sinking velocity that is a saturating function of depth $[S = 50 + (200 - 50)*z/(z + 1,000)]$ to match the result of Berelson (2001). This was necessary to both supply sufficient organic matter remineralization to the Pacific nutricline and prevent excessive supply of organic matter to the deep Pacific sea floor. Sinking rate increases with depth with a half saturation coefficient while lithogenic mineral protection is represented with a constant background flux of 3.85 g m^{-2} yr^{-1} and temperature effect of Laufkötter et al. (2017). Remineralization rates are suppressed under suboxic/anoxic conditions, as a fraction of the rate under fully oxidized conditions. Minimum O_2 concentration for oxic remineralization is enforced to limit O_2 from becoming severely negative. At O_2 concentrations less than this minimum value, anaerobic remineralization occurs. Burial of organic material is set after Dunne et al. (2007) as implemented in COBALT (Stock et al., 2014a) except that a Monod (1949) kinetics with a half saturation length scale 500 m is applied to represent shelf/slope scouring of sediments preventing organic burial.

2.6. Iron Cycling

As in BLINGv1, BLINGv2 takes iron deposition from Fan et al. (2006) and distinguishes between free and inorganically associated iron concentration for scavenging. A global uniform iron ligand concentration of 1 nmol kg^{-1} and equilibrium constant of 500 mol^5 Fe^{-5} kg s^{-1} are taken from Parekh et al. (2005). The ratio of iron efflux from bottom sediment boundaries to the sedimenting phosphorus flux from Elrod et al. (2004) is 0.68 mmol Fe mol C^{-1}, after Moore and Braucher (2008). A 1.5-order iron scavenging is used in order to prevent high iron accumulations in high-deposition regions (like the tropical Atlantic). This also helps prevent Fe accumulating in oligotrophic gyres and in the abyssal ocean where organic fluxes are low. Photodissociation of ligand complexes occurs under bright light, weakening the binding strength (e.g., Barbeau et al., 2001), while at very low iron concentrations, siderophores are thought to be produced as a response to extreme iron stress. Under these assumptions of a spectrum of iron ligands present in seawater with varying binding strengths whose composition varies with light, binding strength is inversely related to both light and iron concentration. Recognizing that in anoxic waters, iron should be reduced, and therefore mostly immune to scavenging, scavenging is turned off when O_2 is less than zero. A 10% efficiency for Fe release from remineralization sinking particles was added and interior scavenging reduced to match the

formulation in COBALT that avoids the otherwise overly strong nutricline peak seen without this modification (Tagliabue et al., 2016).

2.7. External Fluxes

River fluxes of DIC, alkalinity, and PO_4 are specified as globally constant river concentrations that would, at equilibrium, mass balance the observationally based global removal rates through sediment burial of $CaCO_3$ (0.1 PgC yr^{-1}) and organic carbon (0.3 PgC yr^{-1}) in Dunne et al. (2007) under an assumed 1 Sv total global river runoff flux for concentrations of [Alk] = 0.59 mmolC-eq. kg^{-1}, [DIC] = 0.96 mmolC kg^{-1}, and $[PO_4]$ = 6.8 μmolP kg^{-1}. Iron is supplied from the sediment proportional to the supply of sinking organic matter in a fixed ratio. The flux of $CaCO_3$ retained in sediment is calculated using the Dunne et al. (2012) metamodel calibrated to the Hales (2003) steady-state model of $CaCO_3$ burial based on controls on dissolution from bottom water saturation state and organic matter supply. Ultimate burial and dissolution of sediment $CaCO_3$ assumes a 10-cm mixed layer advecting downward at lithogenic and $CaCO_3$-based sediment accumulation rate at steady state every time step. $CaCO_3$ dissolved in the sediment is returned as bottom fluxes of DIC and alkalinity. BLINGv2 updates the equation for $CaCO_3$ burial to be consistent with the values in Dunne et al. (2012). This included raising the global average flux of lithogenic material by over 2 orders of magnitude over the value used in original BLING.

O_2 equilibria and gas exchange follow updated protocols from the sixth phase of the Coupled Model Intercomparison Project (Orr et al., 2017) with CO_2 system equilibrium chemistry after (MOCSY; Orr & Epitalon, 2015) consistent with OCMIP2 protocols (Doney et al., 2004; Najjar & Orr, 1998).

3. Data

3.1. Model Initialization and Spin Up

The model is initialized from World Ocean Atlas 2013 V2 Oxygen (Garcia et al., 2014a) and PO_4 (Garcia et al., 2014b) and Global Data Analysis Project (GLODAP) preindustrial DIC and total alkalinity (Key et al., 2004). Dissolved organic carbon and dissolved iron were initialized from a previous COBALT run. As described in Adcroft et al. (2019), the physical ocean was initialized from a model at rest using temperature and salinity fields from World Ocean Atlas 2013 V2 (Locarnini et al., 2013; Zweng et al., 2013). Due to unfortunate delays in development and time restrictions, the CM4 1850 preindustrial control run was only spun up for 250 years before launching the historical run at year 251. All CM4.0 simulations used externally prescribed concentrations of atmospheric CO_2. To define anthropogenic CO_2 inventories, we compare the CM4.0 preindustrial control and historical runs wherein the CM4.0 control is the preindustrial carbon signal (DIC) and historical run includes the additional anthropogenic signal. Note that this deviates from the ocean biogeochemistry model intercomparison project experimental design of Orr et al. (2017) who argued for a separate anthropogenic CO_2 tracer.

3.2. Data Availability

Model results are available for community analysis via the Earth System Grid Federation (https://esgf-node.llnl.gov/projects/esgf-llnl/) and GFDL's public data server (https://data1.gfdl.noaa.gov/). Many GFDL colleagues and collaborators not included on the author list but who have played invaluable roles in the model workflow and publication of the data are acknowledged through https://doi.org/10.22033/ESGF/CMIP6.1402 website (Guo et al., 2018). The CM4.0 source code is available online (https://doi.org/10.5281/zenodo.3339397).

4. Results

4.1. Drift

As described in Held et al. (2019), CM4.0 conserves tracers in atmosphere, land, sea ice, and ocean to numerical precision. The limits of this conservation are best seen in the case of total salt. In the preindustrial control simulation (piControl), the ESM 4.1 ocean is initialized with 4.7977886009006842 × 1,019 kg of salt and, over the first few years, partitions a small portion of salt into sea ice. After this initial drift, the total ocean salt content over 600 years of piControl through accumulated errors in the numerics made for an overall loss of
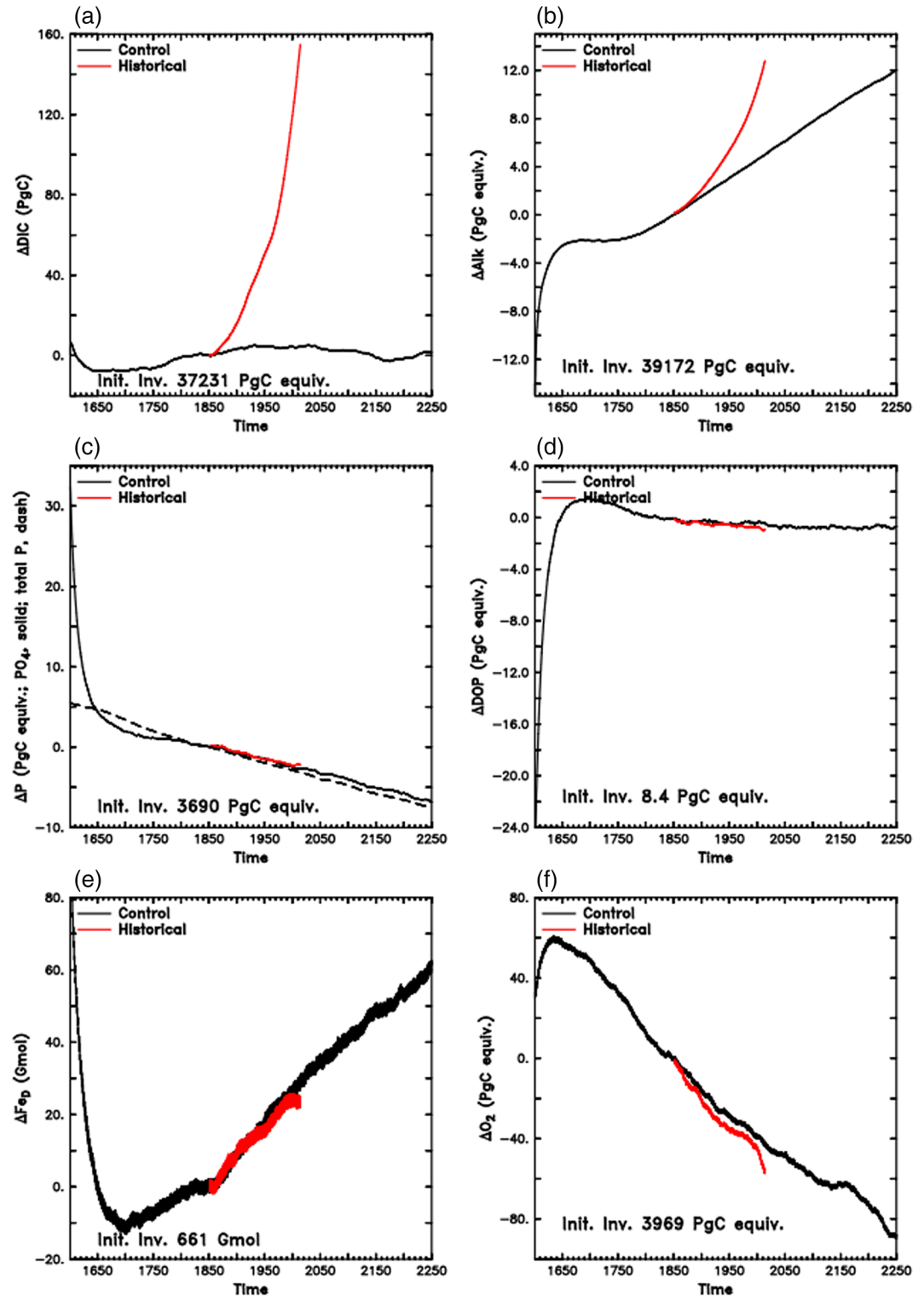
Figure 2. Anomalies in global inventories of all six BLINGv2 prognostic tracers in the control (black) and historical (red) simulations for (a) dissolved inorganic carbon (ΔDIC; PgC), (b) alkalinity (ΔAlk; PgC equivalents), (c) phosphate (PO$_4$; solid as other panels) and phosphate plus dissolved organic phosphorus (total P; dash; both in PgC equivalents using 106:1 ratio), (d) dissolved organic phosphorus (ΔDOP; PgC equivalents), (e) dissolved iron (Fe$_D$; Gmol), and (f) oxygen (PgC equivalents using 106:150 ratio) referenced to the inventory in the control at the year of historical initialization, 1850 (lower right of each panel).
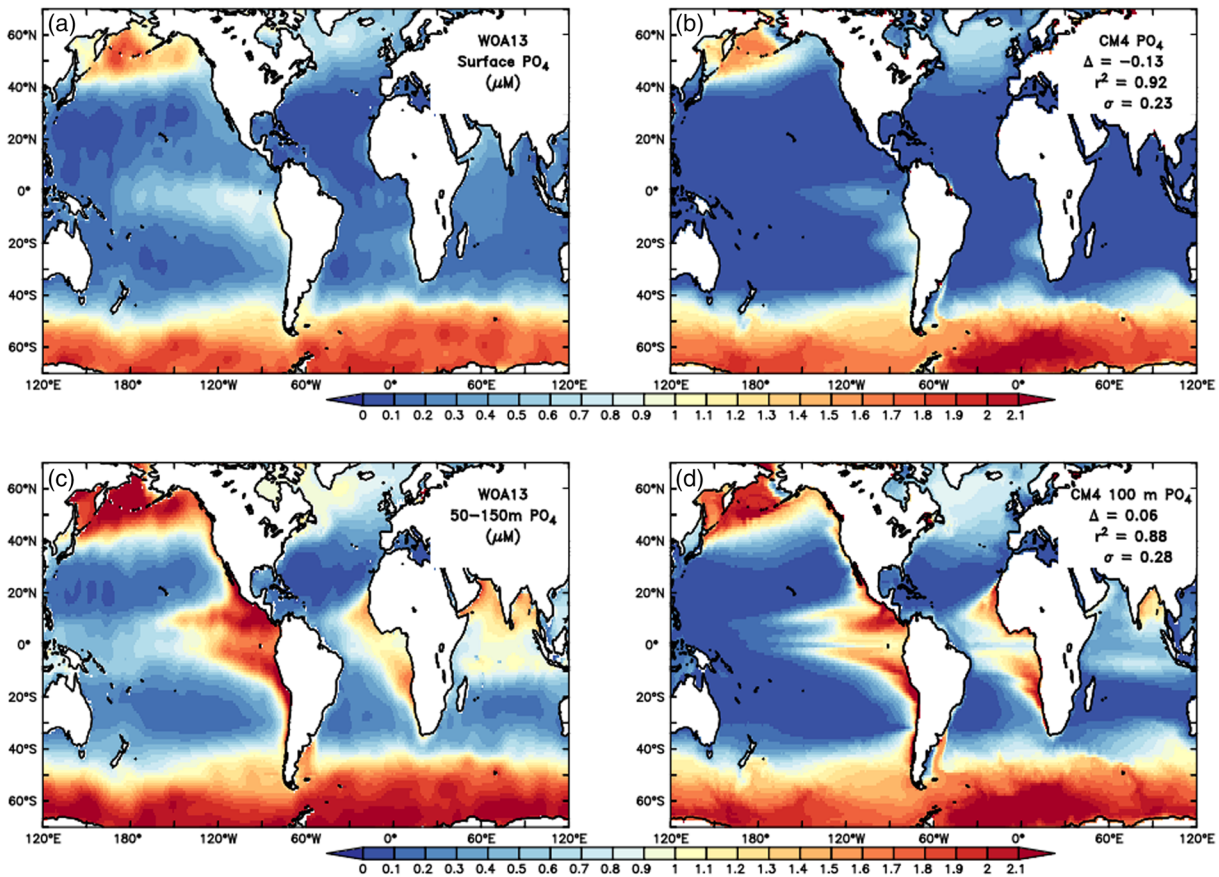
Figure 3. Comparison of PO_4 from World Ocean Atlas 2013 (a, c; Garcia et al., 2014a) with CM4.0 (b, d) at the surface (a, b) and base of the euphotic zone (50–150 m; c, d). Quantification of fidelity is provided as a bias (Δ; µM), squared correlation coefficient (r^2; unitless), and root mean square error (σ; µM).
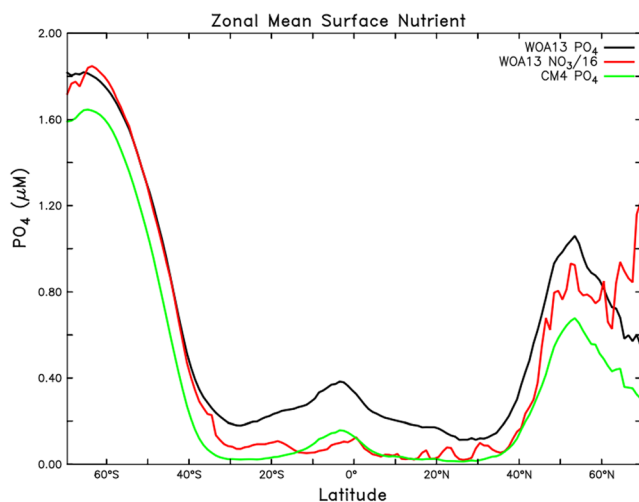

Figure 4. Zonal mean surface concentrations (µM) from World Ocean Atlas 2013 V2 PO_4 (black; Garcia et al., 2014a) and NO_3 divided by 16 (red) along with those from CM4.0 (green).

-1.4×10^{12} kg overall or -2.4×10^9 kg yr^{-1}. While this is a large amount of salt in the absolute sense, it is less than one part in 10 million overall, or less than one part in 10 billion per year which we consider acceptable for such millennial-scale simulations.

As BLINGv2 includes exchanges between tracers and open boundaries, however, biogeochemical inventories are not fixed. Over the CM4 historical run (1850–2014), for example, oceanic carbon is expected to increase because of the added CO_2 forcing. In the control run, the signal is expected to be steady with low variation. With the BLINGv2 representation of river tracer supply and sediment loss, the cycles of PO_4, alkalinity, and inorganic carbon are free to drift (Figure 1). Fortunately, each was near equilibrium as per the 0.1 PgC-eq. yr^{-1} metric of C4MIP for carbon flux (shown in terms of DIC inventory in Figure 2a). In terms of alkalinity (Figure 2b), the control run accumulates alkalinity at a rate of 0.03 PgC-eq. yr^{-1}. However, the two runs start deviating from each other as anthropogenic CO_2 invasion in the historical run promotes dissolution of calcium carbonate such that alkalinity accumulates at a faster rate of 0.08 PgC-eq. yr^{-1}. The PO_4 inventory (Figure 2c) between the two runs is relatively similar, with the control losing 0.014 PgC-eq. yr^{-1} and the historical run 0.018 PgC-eq. yr^{-1} (<0.6% ky^{-1}). Also shown in Figure 2c is the total phosphorus inventory (dash) as the sum of PO_4
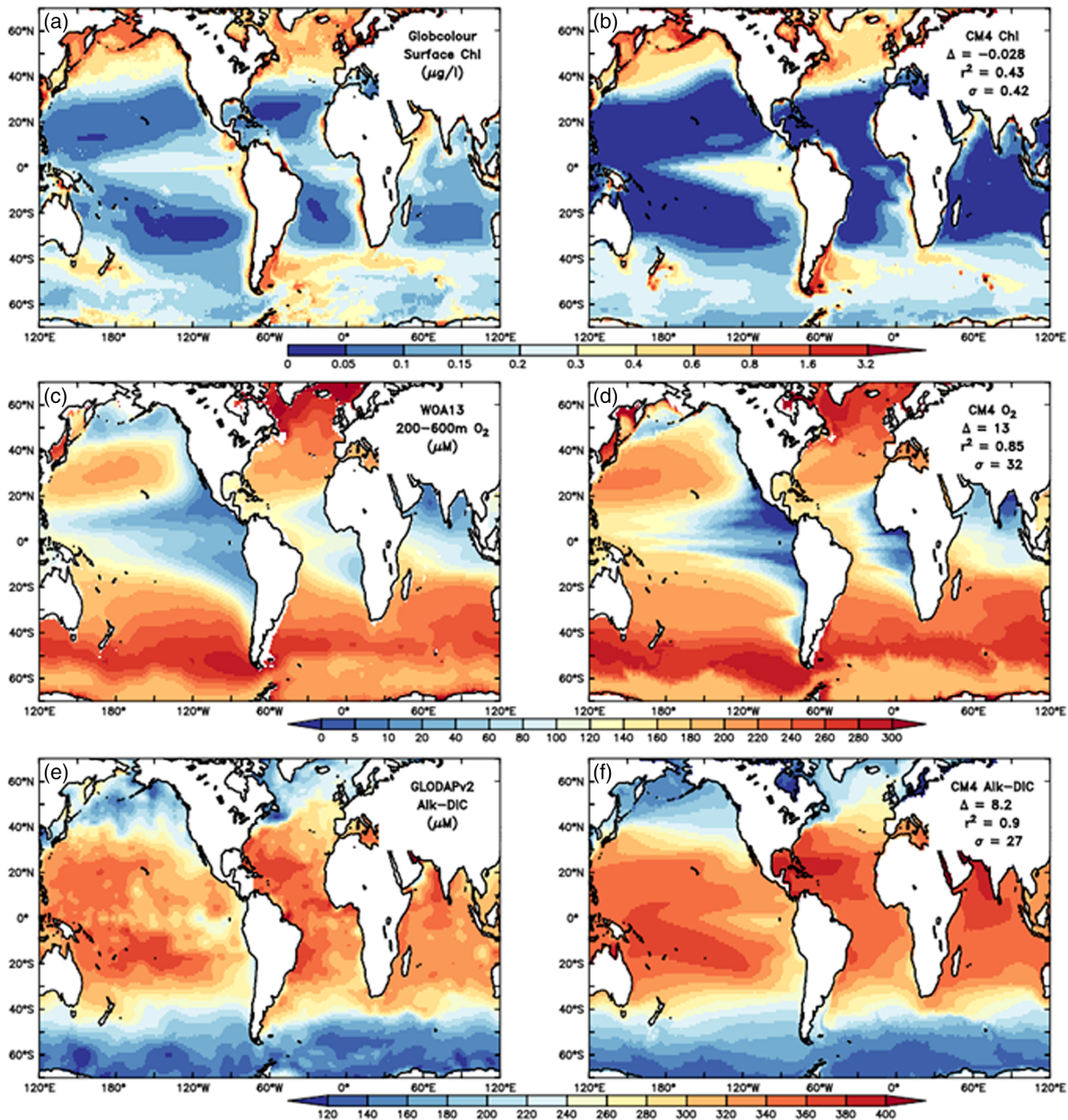
Figure 5. Comparison of surface chlorophyll from a climatology of multisatellite-based ocean color from the GlobColour project (a; Fanton d'Andon et al., 2008) with CM4.0 (b), interior (200–600 m) O_2 from the World Ocean Atlas 2013 (c; Garcia et al., 2014b) and CM4.0 (d), and excess alkalinity (alkalinity minus dissolved inorganic carbon) from GLODAPv2 (e) and CM4.0 (f).

and DOP. The control drift in total phosphorus is approximately 0.02 PgC-eq. yr^{-1}, which is an order of magnitude smaller than the river input (~0.34 PgC-eq. yr^{-1}) and phosphorus burial (~0.33 PgC-eq. yr^{-1}) that should match within numerical precision at equilibrium. As a point of comparison, recent estimates of the ocean phosphorus budget suggest that the preindustrial ocean was losing phosphorus at an order of magnitude higher rate (Wallmann, 2010; 0.15 PgC-eq. yr^{-1} using a conversion of 106:1). DIC increases at a nominal rate of 0.029 PgC-eq. yr^{-1} in the control run and 0.97 PgC-eq. yr^{-1} in the historical run. While the DIC inventory is strongly impacted by anthropogenic CO_2 uptake (Figure 2a) and the alkalinity inventory by the suppression of calcification and calcite burial by acidification (Figure 2b) in the historical run, the other tracer inventories are only modestly impacted relative to their base drift with DOP
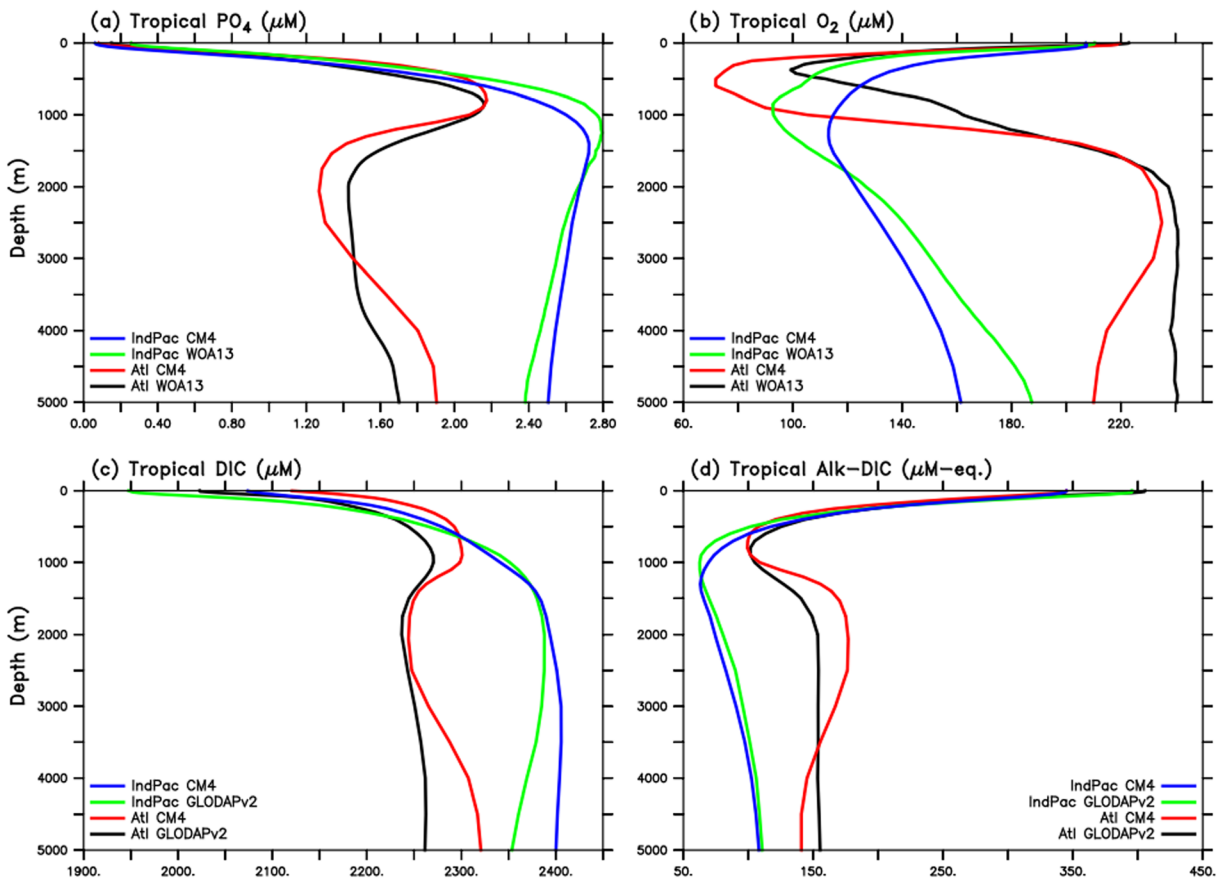
Figure 6. Tropical (30°S to 30°N) basin average concentrations (μM) for PO$_4$ (a), O$_2$ (b), dissolved inorganic carbon (DIC; c), and alkalinity minus DIC (d). World Ocean Atlas PO$_4$ and O$_2$ and GLODAPv2 DIC and alkalinity are shown in black for the Atlantic and green for the Indo-Pacific and CM4.0 in red for the Atlantic and blue for the Indo-Pacific.

decreasing due to decreases in primary production and oxygen declines associated with the combination of solubility and stratification.

4.2. Baseline Comparison to Observations

A quantitative comparison of CM4.0 against other CMIP6 models against observations is performed in Séférian et al. (2020) and in projections in Kwiatkowski et al. (2020). Here we provide comparison with some key observations as background on the CM4.0/BLING key features in this section. We show a comparison of CM4.0 surface PO$_4$ to World Ocean Atlas 2013 observational synthesis in Figure 3 in both the surface and base of the euphotic zone (50–150 m average). Unless otherwise noted, comparisons are made based on model 20-year averages over the 1990–2009 period. The comparison illustrates the strong correspondence of the model to observations in the major oligotrophic gyres, Southern Ocean and equatorial upwelling regions, deep convection regions like the North Atlantic and Sea of Okhotsk, as well as off-equatorial regions such as the eastern tropical Pacific and Eastern Boundary Current regions such as the California, Humboldt, Benguela, and Canary Currents where the nutricline comes close to the surface. Like the previous generation BLINGv1 described in Galbraith et al. (2010), BLINGv2 represents explicit phosphorus cycling without representation of the limitations on nitrogen fixation that would otherwise prevent the complete utilization of phosphate in many areas of the tropical oceans. Overall, the model reproduces 92% of the observed regional variability in surface PO$_4$ and 88% of the observed variability in subsurface PO$_4$. Major weaknesses in the representation of surface PO$_4$ include the overly strong drawdown of PO$_4$ in tropics and subtropics in all oceans but most strongly in the Pacific; lack of high surface PO$_4$ in the eastern Bering Sea, Gulf of Alaska, and Arabian Sea; and overly high PO$_4$ along the coast of Chile and Namibia. It is interesting to note that this bias in coastal Chile is much diminished at the base of the euphotic zone as this region has high PO$_4$ in the
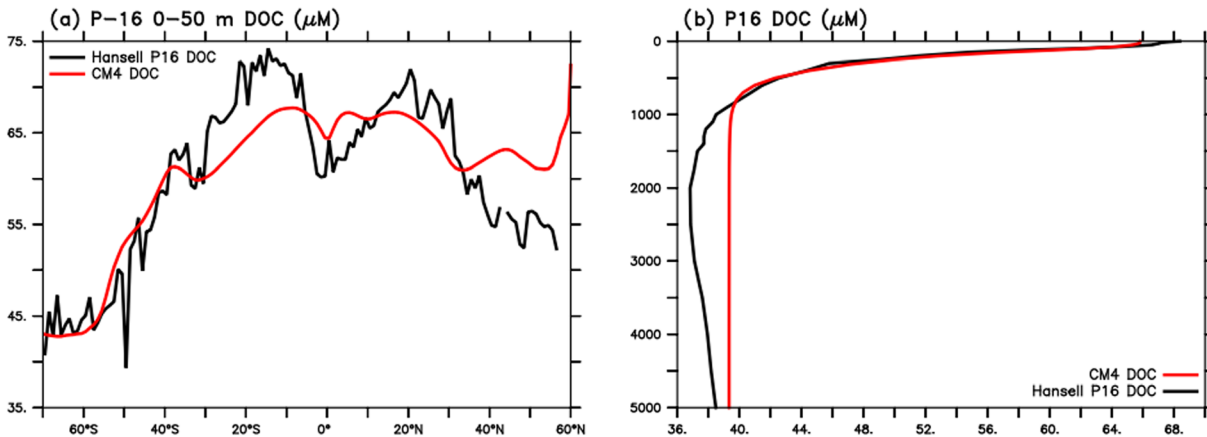
Figure 7. Comparison of dissolved organic carbon from the P16 line (Hansell et al., 2009) with CM4.0 for 155–145°W averaged in the upper 50 m as a function of latitude (a) and as a function of depth (b).

observations as well. Major biases at the base of the euphotic zone (50–150 m; Figures 3c and 3d) include underestimation of high observed PO_4 in the eastern Bering Sea, Gulf of Alaska, Argentinian Shelf, and Arabian Sea and overly high PO_4 in the eastern tropical Atlantic.

The surface nutrient comparison with observations is described further in Figure 4 as zonal mean surface concentrations of PO_4 from World Ocean Atlas 2013 and CM4.0 along with rescaled values of World Ocean Atlas 2013 surface NO_3 divided by 16. While model PO_4 (red) is slightly higher than observations (black) in the Southern Ocean, model PO_4 is consequently drawn down to lower levels than observations in the tropics, similar to what would be expected from a stoichiometrically normalized NO_3 (green line). As such, BLINGv2—like BLINGv1 described in Galbraith et al. (2010)—represents the proximate limitation of productivity by fixed nitrogen rather than true PO_4 distributions throughout the tropics. In the northern subpolar regions, model PO_4 falls in between observations for PO_4 and stoichiometrically normalized NO_3.

Comparison with satellite chlorophyll from the GlobColour project (Fanton d'Andon et al., 2008) and interior (200–600 m) O_2 from World Ocean Atlas 2013 (Garcia et al., 2014b) is shown in Figure 5. Chlorophyll in CM4.0 represents most of the major features in satellite observations but exhibits an exaggerated contrast between eutrophic and oligotrophic conditions with high chlorophyll being highly focused directly over areas of upwelling and chlorophyll away from upwelling sites being artificially low. This is a direct consequence of the steady-state ecosystem assumptions and presence of only a single organic material pool with
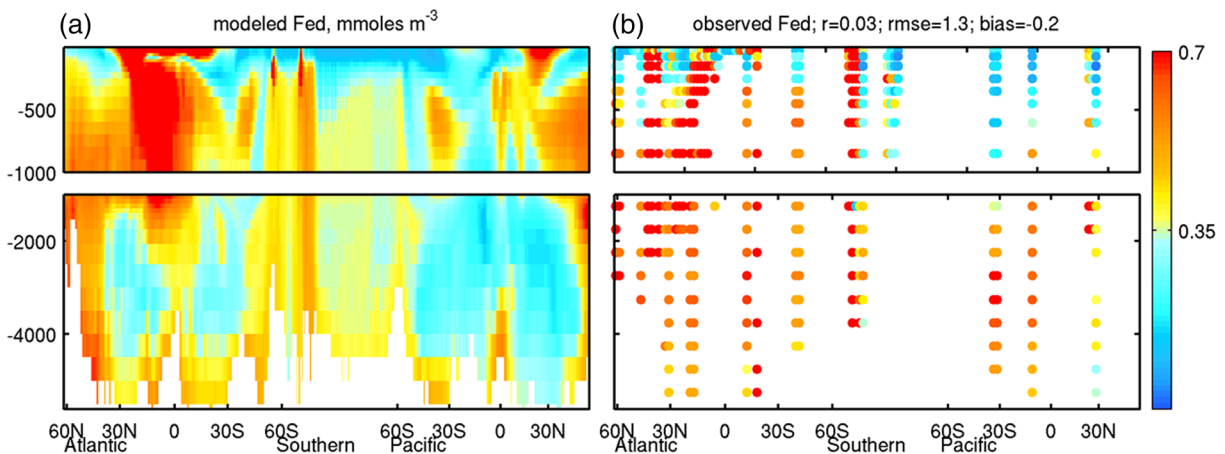

Figure 8. Comparison of dissolved iron (Fe_D; mmol m-3) in CM4.0 (a) and the synthesis of observations by Tagliabue et al. (2016) (b). Skill assessment was based on first mapping onto a 1×1 grid before taking the mean of observations falling into grid cells from a swath running along the transect with a total with of five grid cells (i.e., the grid cell directly on the transect and two grid cells in either direction perpendicular to the transect). Averages were smoothed over 250 km to highlight large-scale patterns.
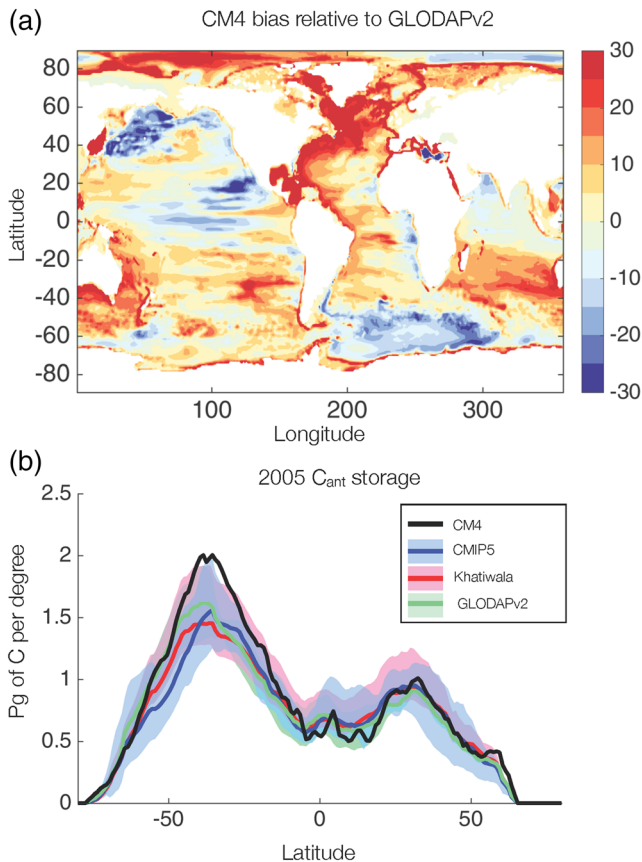
Figure 9. Difference in upper 2,000 m oceanic anthropogenic carbon between years 2000 and 2010 of the CM4.1 historical simulation and GLODAPv2 (a), where the GLODAPv2 data have been adjusted to an 1850 start date following Bronselaer et al. (2017). Zonal integral of oceanic anthropogenic carbon content (year 2000–2010 mean; b) from CM4.0 (black), CMIP5 mean (Bronselaer et al., 2017; blue), and observational estimates from Khatiwala et al. (2012; red), GLODAPv2 (green). The red and green shading indicate the one standard deviation range in observational uncertainty. The blue line shows the CMIP5 mean for the models used in Bronselaer et al. (2017), with the blue-shaded region showing the full model spread. All data plotted have been adjusted to an 1850 start date for measuring anthropogenic carbon.

a relative residence time (18 years) compared to ecosystem time scales. Similarly, interior O_2 patterns compare well with observations, overall capturing 85% of the regional variation, but exhibit overexpression of hypoxia in the eastern basin of all oceans and a high bias of 13 µM. In the lower panels, we show comparison of GLODAPv2 (Olsen et al., 2016) surface excess alkalinity (Figure 4e) with CM4.0 surface excess alkalinity (Figure 5f). CM4.0 captures 90% of the regional variation in excess alkalinity with a slight high bias 8.2 µM equivalents.

To compare the vertical structure correspondence of biogeochemical patterns in observations (black) and CM4.0 (red), we separate the distributions into tropical basin averages for the Indo-Pacific (solid) and Atlantic (dash) in Figure 6. In the tropical Atlantic (Figure 5, dashed lines), the vertical structure of model PO_4 compares well with observations with respect to the amplitude and depth of the nutricline peak though the model has too much PO_4 at the bottom (below 4,000 m) at the expense of the abyss (2,000–4,000 m). Similarly, the associated depth structure of tropical Atlantic O_2 (Figure 6b), DIC (Figure 6c), and excess alkalinity (Figure 6d) thermocline, abyssal, and bottom features are all well represented but arguably overexpressed. In the Indo-Pacific (Figure 6, solid lines), the model nutricline (Figure 6a) and oxycline (Figure 6b) are overly deep and underexpressed (i.e., subsurface maximum PO_4 and minimum O_2 are not as strong as in observations). These biases map onto the DIC (Figure 6c) and excess alkalinity (Figure 6d) structure in part, but both remain fairly well represented. Note that as the model has only run 400 years in this analysis, deep Pacific biases are still evolving while Atlantic biases have roughly come to equilibrium.

The highest excess alkalinity values occur in the surface layers, where biology plays a large role in anthropogenic carbon uptake. Below the surface layer, downwelling associated with gyre circulation carries carbon further into the ocean basin, followed by mode and intermediate water formation (~850–1,250 m). Below 1,250 m, the Atlantic Meridional Overturning Circulation (AMOC) and deep convection carries the remaining anthropogenic carbon downward. Variability at depth (~5,000 m) could be attributed to the short model run time. To fully constrain deep ocean processes, the model should be run for a longer time frame, as deep ocean processes happen over millennia—something that was beyond our computational abilities for these experiments. Lastly, in agreement with observations, anthropogenic carbon penetration is deeper in the North Atlantic and the Southern Ocean, due to excess alkalinity and deeper mixed layers caused by mixing and deep-water formation.

As shown in Figure 2, all tracer inventories in CM4.0 are undergoing significant drift and are not at a true equilibrium state with respect to external sources and sinks. As discussed in Séférian et al. (2016), the level of incompleteness of spin up toward equilibrium can have important implications for model performance and transient response to changed forcing. Specifically, the short spin up can make the model appear more representative of observations than if it were run to equilibrium. For example, we expect from biases in overextension of tropical Pacific hypoxia shown in Figures 5 and 6 and associated global decline in oxygen (Figure 2) to continue to grow, further decreasing model fidelity and representativeness of the resulting transient change. Other implications for ecosystem and biogeochemical response are less clear.

Comparison of modeled dissolved organic carbon with observations from Hansell et al. (2009) for the P16 transect is shown at the surface as a function of latitude in Figure 7a. While CM4.0 underrepresents the equatorial to subtropical gradient in surface DOC, it represents well the overall tropical to subpolar gradient in the Southern Hemisphere. Unfortunately, CM4.0 does not capture the relatively low values in the
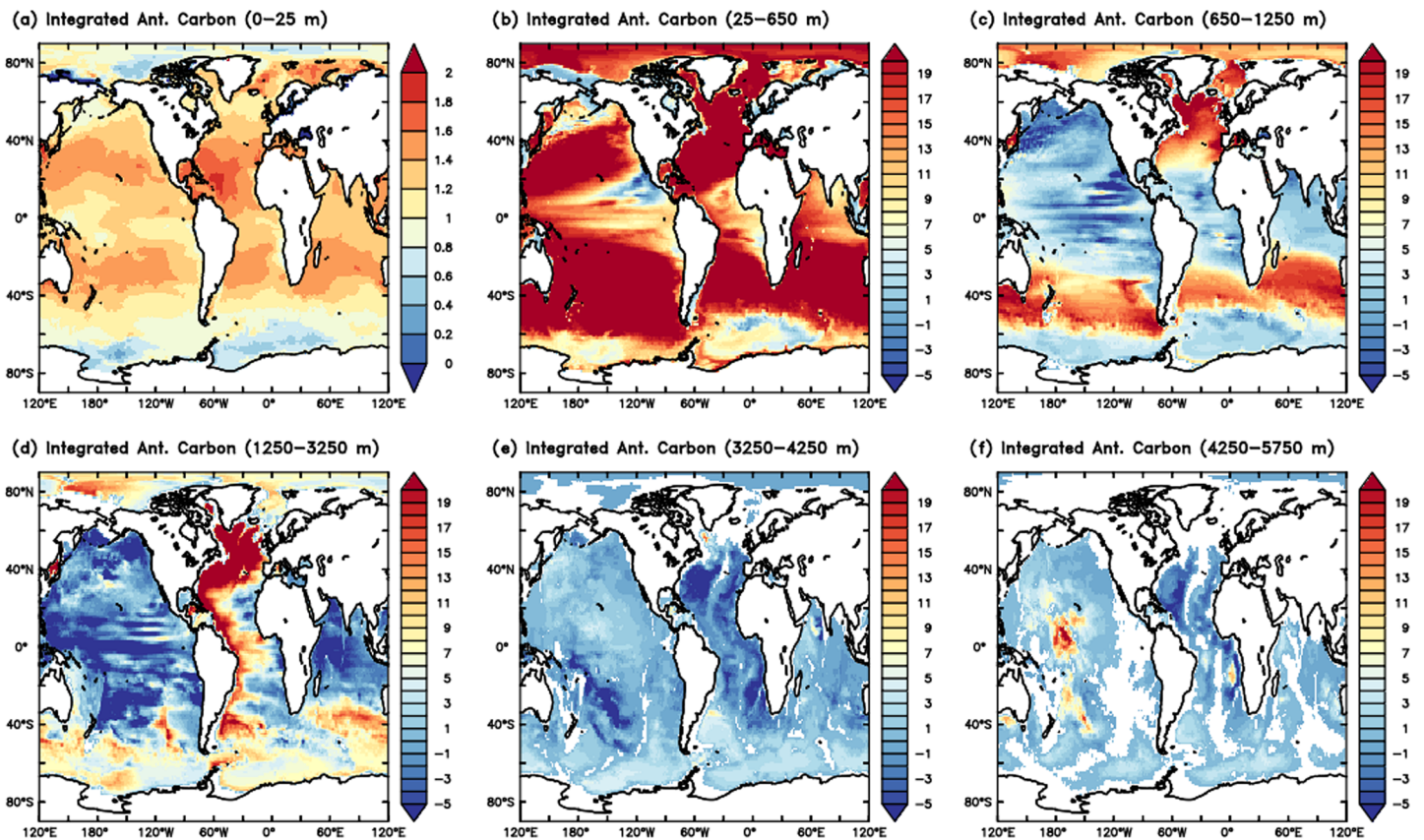
Figure 10. Anthropogenic carbon integrated within depth zones from the surface (a; 0–25 m), upper thermocline (b; 25–650 m), lower thermocline (c; 650–1,250 m), deep ocean (d; 1,250–3,250 m), abyss (e; 3,250–4,250 m), and bottom (f; 4,250–5,750 m).

subpolar North Pacific. Average DOC along P16 is shown as a function of depth in Figure 7b illustrating the good correspondence of the primary DOC gradient in the thermocline. As BLINGv2 assumes a constant 38 μM offset of refractory DOC, it does not capture any of the ocean conveyor time scale dynamics of DOC in the deep ocean, however.

Comparison of CM4.0 (Figure 8a) with observations (Figure 8b) of dissolved iron is less robust than for other tracers, in part because of the limited available data set, but also because of the complexities involved. As discussed in Tagliabue et al. (2016), observed iron distributions are a result of a complex interplay of not only nutrient cycling but also strong local and regional patterns of atmospheric deposition, scavenging, coastal and benthic supply, and hydrothermal activity. While CM4.0 is able to capture the general elevation of North Atlantic over the Pacific associated with atmospheric deposition and nutrient-like behavior, the primary CM4.0 pattern was low with patchy highs at the surface followed by generally high values at depth near coasts and low values in the interior. As discussed in Tagliabue et al. (2016), this is a common bias in models that ignore the interior hydrothermal source for iron and suggests that abyssal scavenging in BLINGv2 is too strong. The correspondence with observations is weak in the upper 1,000 m ($r = 0.17$) but poor overall ($r = 0.03$).

4.3. Anthropogenic Carbon Uptake

To calculate oceanic anthropogenic carbon, the CM4.0 control run DIC was subtracted from the CM4.0 historical run. Over the 1850–2014 period of the historical run, the total modeled oceanic anthropogenic carbon is 109.5 PgC, with 91.5% in the upper 1,500 m of the water column. As shown in Figure 9a, much of the high bias in CM4.1 relative to GLODAPv2 is exhibited in the North Atlantic deep western boundary and southern subtropics surrounding Australia. As shown in Figure 9b, the CM4.0 anthropogenic carbon uptake as a function of latitude exhibits a high bias relative to reanalysis efforts by GLODAPv2 (green; Khatiwala et al., 2012,
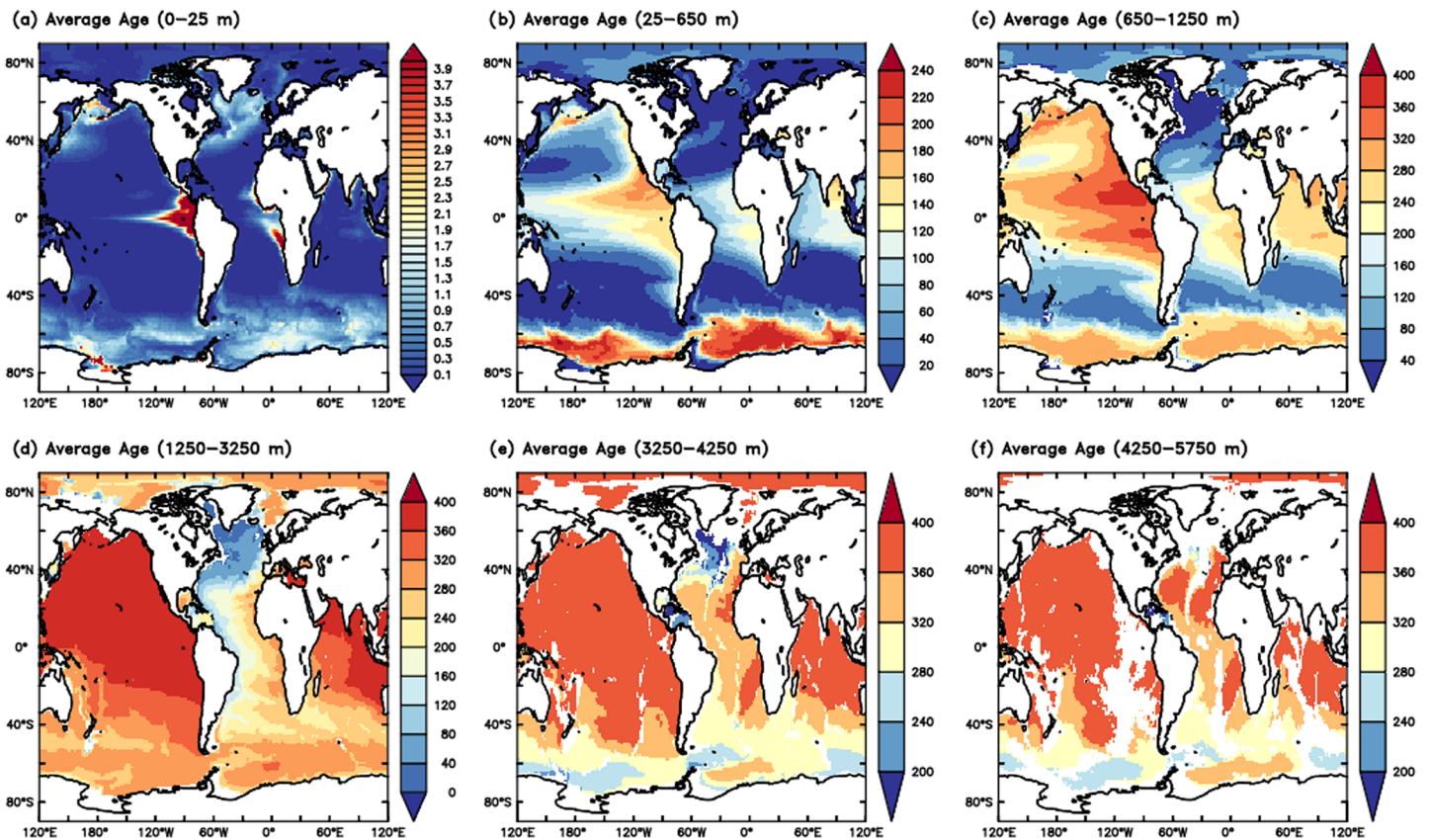
Figure 11. Ideal age tracer within depth zones from the surface (a; 0–25 m), upper thermocline (b; 25–650 m), lower thermocline (c; 650–1,250 m), deep ocean (d; 1,250–3,250 m), abyss (e; 3,250–4,250 m), and bottom (f; 4,250–5,750 m).

red) and the CMIP5 ensemble (Bronselaer et al., 2017; blue). High uptake of carbon in the Southern Ocean is partially explained by the lack of sufficiently resolving the role of eddy-induced re-stratification and intentional omission of a thickness mixing parameterization in CM4.0 (Adcroft et al., 2019). This lack of eddy resolution results in a spurious enhancement in ventilation in the Southern Ocean mode and interior water formation regions. Separate analysis of CM4.0 chlorofluorocarbon distributions compared to observations (Dunne et al., 2020) highlights bias of up to 50% in the 700- to 2,000-m depth range between 35°S and 50°S resulting from this spurious enhancement in ventilation. We thus consider the enhanced anthropogenic CO_2 uptake in this region similarly spurious and an important topic of future model development at ¼° resolution.

4.4. Anthropogenic Carbon Patterns and Relation to Ideal Age

To explain the CM4.0 regional and depth patterns in anthropogenic carbon, we illustrate integrated maps across the surface, upper thermocline, lower thermocline, abyss, and bottom depth intervals in Figure 10. In the surface, anthropogenic carbon patterns largely reflect the distribution of buffering capacity as expressed by excess alkalinity (Figure 6). The highest excess alkalinity values occur in the surface layers (Figure 10a), where biology plays a large role in anthropogenic carbon uptake. Below the surface layer, patterns in anthropogenic carbon largely follow patterns in ideal age (Thiele & Sarmiento, 1990; Figure 11), a tracer that is set to 0 at initialization and returned to 0 at the surface and increase with integration time to act as a clock with respect to ventilation at the surface. Interior water parcels become "older" over time; however, the potential for bias increases at depth because of model run time, in this case 400 years. While ideal age is not a true observable per se, it does reflect patterns in other observables of ocean ventilation such as chlorofluorocarbons and apparent oxygen utilization. In the upper thermocline (Figure 10b), downwelling associated with gyre circulation carries carbon further into the ocean basin. In the lower thermocline (Figure 10c), anthropogenic carbon patterns follow mode and intermediate water formation pathways

Table 1

Summary of Anthropogenic Carbon Content Contributions to the Total (%) at Various Depth Levels and Statistical Explanatory Power of Ideal Age, Apparent Oxygen Utilization (AOU), and Excess Alkalinity as Squared Regression Coefficient With the Modeled Spatial Patterns of Anthropogenic Carbon at Each Level

	(0–25 m)	(25–650 m)	(650–1,250 m)	(1,250–3,250 m)	(3,250–4,250 m)	(4,250–5,750 m)
Carbon content (%)	4.28	60.98	20.06	12.23	0.30	2.05
Age (R^2)	0.03	0.19	0.62	0.49	0.03	0.003
AOU (R^2)	0.07	0.19	0.54	0.29	0.02	0.04
Excess Alk (R^2)	0.42	0.73	0.47	0.21	0.02	0.11

(~850–1,250 m). As noted in Adcroft et al. (2019), this is the region where the CM4.0 representation of explicit but not parameterized eddies leads to an overexpression of ventilation and overly high anthropogenic carbon uptake compared to observations as shown in Figure 9. Below 1,250 m, anthropogenic carbon patterns largely reflect the AMOC (Figure 10d) as deep convection carries the remaining anthropogenic carbon downward. Little anthropogenic carbon makes it into the abyss (Figure 10e). Patches of high apparent anthropogenic carbon at the bottom of the central North Pacific (~5,000 m; Figure 10f) are most likely a result of subsidence of water masses associated with a decrease in Antarctic bottom water formation (Purkey & Johnson, 2012). Strongly zonal patterns develop across tropical Pacific in the 650- to 3,250-m
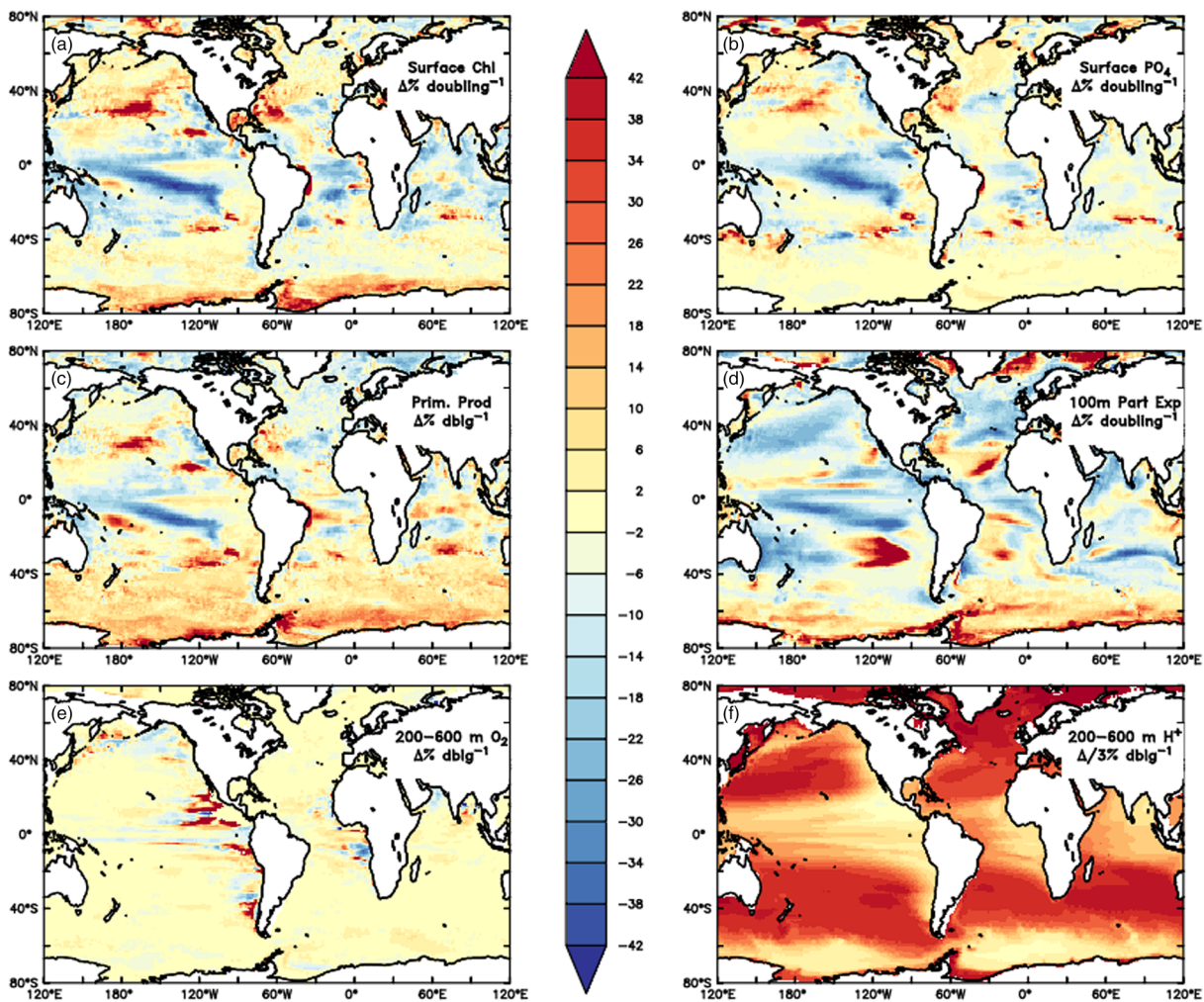

Figure 12. Percent change in response to a doubling of CO_2 [(years 131–150 minus years 1–20)/(2 × years 1–20)*100] for surface chlorophyll (a), surface PO_4 (b), integrated primary production (c), particle export past 100 m (d), and average oxygen (e) and hydrogen ion concentration (f) in the 200- to 600-m range. Note that in the case of hydrogen ion concentration, the variable was additionally divided by 3 to conform to the same scale as the other variables.

depth range (Figures 10c and 10d). These patterns develop in the differences between natural and anthropogenic carbon as changes in the position and intensity of equatorial fronts and associated zonal currents under historical climate changes in this zonal of strong zonal currents and meridional gradients. Lastly, as in observations, anthropogenic carbon penetration is deeper in the North Atlantic and the Southern Ocean, due to excess alkalinity and deeper mixed layers caused by mixing and deep-water formation. The quantitative results of the partitioning of anthropogenic carbon inventory and pattern variance explained by ideal age (Figure 11) and apparent oxygen utilization are summarized in Table 1.

As a preliminary analysis of the sensitivity of this model to greenhouse gas warming, we present a few key metrics of ocean biogeochemical change under one of the DECK experiments idealized warming scenario of 1% yr^{-1} increase of atmospheric CO_2 to quadrupling in Figure 12. Similar to the CMIP5 series of models (Bopp et al., 2013), CM4.0 exhibits a general decrease in surface chlorophyll (Figure 12a) and nutrients (Figure 12b) and associated productivity (Figure 10c) and particle export (Figure 12d) metrics with intensely regional variability and many areas of increase. We also see considerable amplification of these changes in moving from chlorophyll, PO_4, and primary production (Figures 12a–12c) through food web interactions to particle export (Figure 12d). This result is similar to the manifestation of trophic amplification described in detail in Stock et al. (2014b) as temperature drives an increase in physiological rates but reduced nutrient supply drives that increase into the microbial loop (Laufkötter et al., 2015, 2016). Much of the areas that exhibit decreases are associated with a constriction of the expanse of unutilized nutrient after having been upwelled to the surface such as in the equatorial Pacific high-nutrient, low-chlorophyll zone. Patterns of particle export exhibit particularly strong decreases in midlatitudes associated with decreases in wintertime deep mixing. The Southern Ocean exhibits considerable increase in particle export along the Antarctic continent. Modeled O_2 (Figure 12e) changes very little as decreases in interior remineralization rates roughly balance reductions associated with solubility. Interior increase in hydrogen ion concentration is extreme, with increase up to a factor of 3 as CO_2 doubles, most notably in the subtropical gyres and North Atlantic subpolar and Arctic regions.

5. Conclusions

GFDL's CM4.0 includes major improvements in the physical climatology and modes of variability from previous GFDL models (Held et al., 2019) and, through the incorporation of BLINGv2, additionally provides a simple yet robust representation of the carbon cycle. Comparison of surface and subsurface biogeochemical properties and anthropogenic carbon compares well with observations. For example, comparison with chlorophyll distributions demonstrates that this ¼° of MOM6 ocean represents key features of coastal chlorophyll and O_2 distributions as these are influenced by boundary currents and shelf interactions. We expect that high-resolution modeling approaches in this class model will afford a wave of new insights on coastal large-scale interactions given the high coastal residence times now capable of being represented (Liu et al., 2019). Major deficiencies in CM4.0 biogeochemistry include the inability to distinguish between the major nutrient cycles of phosphorus and nitrogen (Figure 4) and spurious uptake of anthropogenic carbon associated with overly strong upper ocean ventilation near 40°S (Figure 9) which is also seen in chlorofluorocarbon tracers (Dunne et al., 2020).

We describe the central mechanisms driving anthropogenic carbon uptake in CM4.0 (Figures 10 and 11 and Table 1). The highest anthropogenic carbon uptake is associated with the highest excess alkalinity values which occur in the surface layers. Below the surface layer, downwelling associated with gyre circulation carries carbon further into the ocean basin, followed by mode and intermediate water formation (~850–1,250 m). Below 1,250 m, the AMOC and deep convection carry the remaining anthropogenic carbon downward. As in observations, anthropogenic carbon penetration is deeper in the North Atlantic and the Southern Ocean, due to excess alkalinity and deeper mixed layers caused by mixing and deep-water formation. We also present preliminary analysis of ocean biogeochemical response to idealized CO_2-induced climate warming that highlights the role of enhanced stratification in reduction of nutrient supply and associated particle export out of the surface ocean (Figure 12). The structure of this decrease suggests a strong reduction in the area of elevated nutrient following equatorial upwelling and general tropical decline under climate warming but also illustrates the complex interplay of processes at work in the Southern Ocean, consistent with results from previous studies.

In its ability to represent interior ocean biogeochemical interactions with ocean eddies under climate variability and anthropogenic change, CM4.0 provides a major advance in coupled carbon-climate interactions through a combination of improved resolution and algorithmic development. Areas of future development include longer model runs and efforts to resolve the role of eddy-induced restratification through either improved eddy parameterization or additionally increased resolution to enhance modeled ocean anthropogenic carbon fidelity over depth and time.

Data Availability Statement

CM4.0 data are available at doi.org/10.22033/ESGF/CMIP6.1402 website. The CM4.0 source code is available online (https://doi.org/10.5281/zenodo.3339397).

References

Abell, J., Emerson, S., & Rebaud, P. (2000). Distributions of TOP, TON and TOC in the North Pacific subtropical gyre: Implications for nutrient supply in the surface ocean and remineralization in the upper thermocline. *Journal of Marine Research*, *58*(2), 203–222. https://doi.org/10.1357/002224000321511142

Adcroft, A., Anderson, W., Balaji, V., Blanton, C., Bushuk, M., Dufour, C. O., et al. (2019). The GFDL Global Ocean and Sea Ice Model OM4.0: Model description and simulation features. *Journal of Advances in Modeling Earth Systems*, *11*(10), 3167–3211. https://doi.org/10.1029/2019MS001726

Anderson, L. A. (1995). On the hydrogen and oxygen content of marine phytoplankton. *Deep-Sea Research Part I*, *42*, 1675–1680.

Archer, D. E., & Johnson, K. (2000). A model of the iron cycle in the ocean. *Global Biogeochemical Cycles*, *14*(1), 269–279. https://doi.org/10.1029/1999GB900053

Bacastow, E., & Maier-Reimer, E. (1990). Ocean-circulation model of the carbon cycle. *Climate Dynamics*, *4*(2), 95–125. https://doi.org/10.1007/BF00208905

Barbeau, K., Rue, E. L., Bruland, K. W., & Butler, A. (2001). Photochemical cycling of iron in the surface ocean mediated by microbial iron (III)-binding ligands. *Nature*, *413*(6854), 409–413. https://doi.org/10.1038/35096545

Berelson, W. M. (2001). Particle settling rates increase with depth in the ocean. *Deep Sea Research Part II: Topical Studies in Oceanography*, *49*(1–3), 237–251. https://doi.org/10.1016/S0967-0645(01)00102-3

Bissinger, J. E., Montagnes, D. J., & Atkinson, D. (2008). Predicting marine phytoplankton maximum growth rates from temperature: Improving on the Eppley curve using quantile regression. *Limnology and Oceanography*, *53*(2), 487–493. https://doi.org/10.4319/lo.2008.53.2.0487

Bopp, L., Monfray, P., Aumont, O., Dufresne, J. L., le Treut, H., Madec, G., et al. (2001). Potential impact of climate change on marine export production. *Global Biogeochemical Cycles*, *15*(1), 81–99. https://doi.org/10.1029/1999GB001256

Bopp, L., Resplandy, L., Orr, J. C., Doney, S. C., Dunne, J. P., Gehlen, M., et al. (2013). Multiple stressors of ocean ecosystems in the 21st century: Projections with CMIP5 models. *Biogeosciences*, *10*(10), 6225–6245. https://doi.org/10.5194/bg-10-6225-2013

Bronselaer, B., Winton, M., Russell, J., Sabine, C. L., & Khatiwala, S. (2017). Agreement of CMIP5 simulated and observed ocean anthropogenic CO_2 uptake. *Geophysical Research Letters*, *44*, 12–298. https://doi.org/10.1002/2017GL074435

Doney, S. C., Fabry, V. J., Feely, R. A., & Kleypas, J. A. (2009). Ocean acidification: The other CO_2 problem. *Annual Review of Marine Science*, *1*(1), 169–192. https://doi.org/10.1146/annurev.marine.010908.163834

Doney, S. C., Lindsay, K., Caldeira, K., Campin, J. M., Drange, H., Dutay, J. C., et al. (2004). Evaluating global ocean carbon models: The importance of realistic physics. *Global Biogeochemical Cycles*, *18*, GB3017. https://doi.org/10.1029/2003GB002150

Doney, S. C., Lindsay, K., Fung, I., & John, J. (2006). Natural variability in a stable, 1000-yr global coupled climate-carbon cycle simulation. *Journal of Climate*, *19*(13), 3033–3054. https://doi.org/10.1175/JCLI3783.1

Dunne, J. P., Armstrong, R. A., Gnanadesikan, A., & Sarmiento, J. L. (2005). Empirical and mechanistic models for the particle export ratio. *Global Biogeochemical Cycles*, *19*, GB4026. https://doi.org/10.1029/2004GB002390

Dunne, J. P., Hales, B., & Toggweiler, J. R. (2012). Global calcite cycling constrained by sediment preservation controls. *Global Biogeochemical Cycles*, *26*, GB3023. https://doi.org/10.1029/2010GB003935

Dunne, J. P., Horowitz, L. W., Adcroft, A. J., Ginoux, P., Held, I. M., John, J. G., et al. (2020). The GFDL Earth System Model version 4.1 (GFDL-ESM 4.1): Model description and simulation characteristics. *Journal of Advances in Modeling Earth Systems*. https://doi.org/10.1029/2019MS002015

Dunne, J. P., John, J. G., Shevliakova, E., Stouffer, R. J., Krasting, J. P., Malyshev, S. L., et al. (2013). GFDL's ESM 2 global coupled climate-carbon earth system models. Part II: Carbon system formulation and baseline simulation characteristics. *Journal of Climate*, *26*(7), 2247–2267. https://doi.org/10.1175/JCLI-D-12-00150.1

Dunne, J. P., Sarmiento, J. L., & Gnanadesikan, A. (2007). A synthesis of global particle export from the surface ocean and cycling through the ocean interior and on the seafloor. *Global Biogeochemical Cycles*, *21*, GB4006. https://doi.org/10.1029/2006GB002907

Dutkiewicz, S., Follows, M. J., & Parekh, P. (2005). Interactions of the iron and phosphorus cycles: A three-dimensional model study. *Global Biogeochemical Cycles*, *19*, GB1021. https://doi.org/10.1029/2004GB002342

Elrod, V. A., Berelson, W. M., Coale, K. H., & Johnson, K. S. (2004). The flux of iron from continental shelf sediments: A missing source for global budgets. *Geophysical Research Letters*, *31*, L12307. https://doi.org/10.1029/2004GL020216

Eppley, R. W. (1972). Temperature and phytoplankton growth in the sea. *Fishery Bulletin*, *70*(4), 1063–1085.

Eyring, V., Bony, S., Meehl, G. A., Senior, C. A., Stevens, B., Stouffer, R. J., & Taylor, K. E. (2016). Overview of the Coupled Model Intercomparison Project Phase 6 (CMIP6) experimental design and organization. *Geoscientific Model Development*, *9*(5), 1937–1958. https://doi.org/10.5194/gmd-9-1937-2016

Fan, S. M., Moxim, W. J., & Levy, H. (2006). Aeolian input of bioavailable iron to the ocean. *Geophysical Research Letters*, *33*, L07602. https://doi.org/10.1029/2005GL024852

Fanton d'Andon, O. H., Antoine, D., Mangin, A., Maritorena, S., Durand, D., Pradhan, Y., et al. (2008). Ocean colour sensors characterisation and expected error estimates of ocean colour merged products from GlobColour. In *Ocean Optics XIX* (pp. 1–51). Barga, Italy.

Friedlingstein, P., Cox, P., Betts, R., Bopp, L., von Bloh, W., Brovkin, V., et al. (2006). Climate-carbon cycle feedback analysis: Results from the C4MIP model intercomparison. *Journal of Climate*, *19*(14), 3337–3353. https://doi.org/10.1175/JCLI3800.1

Frölicher, T. L., Sarmiento, J. L., Paynter, D. J., Dunne, J. P., Krasting, J. P., & Winton, M. (2015). Dominance of the Southern Ocean in anthropogenic carbon and heat uptake in CMIP5 models. *Journal of Climate*, *28*(2), 862–886. https://doi.org/10.1175/JCLI-D-14-00117.1

Galbraith, E. D., Dunne, J. P., Gnanadesikan, A., Slater, R. D., Sarmiento, J. L., Dufour, C. O., et al. (2015). Complex functionality with minimal computation: Promise and pitfalls of reduced-tracer ocean biogeochemistry models. *Journal of Advances in Modeling Earth Systems*, *7*, 2012–2028. https://doi.org/10.1002/2015MS000463

Galbraith, E. D., Gnanadesikan, A., Dunne, J. P., & Hiscock, M. R. (2010). Regional impacts of iron-light colimitation in a global biogeochemical model. *Biogeosciences*, *7*(3), 1043–1064. https://doi.org/10.5194/bg-7-1043-2010

Garcia, H. E., Locarnini, R. A., Boyer, T. P., Antonov, J. I., Baranova, O. K., Zweng, M. M., et al. (2014a). *World Ocean Atlas 2013, volume 3: Dissolved oxygen, apparent oxygen utilization, and oxygen saturation*. In S. Levitus & A. Mishonov (Eds.), *NOAA Atlas NESDIS 75* (pp. 1–27).

Garcia, H. E., Locarnini, R. A., Boyer, T. P., Antonov, J. I., Baranova, O. K., Zweng, M. M., et al. (2014b). *World Ocean Atlas 2013, Volume 4: Dissolved inorganic nutrients (phosphate, nitrate, silicate)*. In S. Levitus & A. Mishonov (Eds.), *NOAA Atlas NESDIS 76* (pp. 1–25).

Geider, R. J., MacIntyre, H. L., & Kana, T. M. (1997). Dynamic model of phytoplankton growth and acclimation: Responses of the balanced growth rate and the chlorophyll a:carbon ratio to light, nutrient-limitation and temperature. *Marine Ecology Progress Series*, *148*, 187–200. https://doi.org/10.3354/meps148187

Griffies, S. M., Gnanadesikan, A., Dixon, K. W., Dunne, J. P., Gerdes, R., Harrison, M. J., et al. (2005). Formulation of an ocean model for global climate simulations. *Ocean Science*, *1*(1), 45–79. http://www.ocean-sci.net/1/45/2005/, https://doi.org/10.5194/os-1-45-2005

Guo, H., John, J. G., Blanton, C., McHugh, C., Nikonov, S., Radhakrishnan, A., et al. (2018). *NOAA-GFDL GFDL-CM4 model output prepared for CMIP6 CMIP 1pctCO₂*. Earth System Grid Federation. https://doi.org/10.22033/ESGF/CMIP6.8470

Hallberg, R. W. (2014). Numerical instabilities of the ice/ocean coupled system. *CLIVAR Exchanges 65*, *19*(2), 38–42. http://www.clivar.org/sites/default/files/documents/exchanges65_0.pdf

Hales, B. (2003). Respiration, dissolution, and the lysocline. *Paleoceanography*, *18*(4). https://doi.org/10.1029/2003PA000915

Hansell, D. A., Carlson, C. A., Repeta, D. J., & Schlitzer, R. (2009). Dissolved organic matter in the ocean: A controversy stimulates new insights. *Oceanography*, *22*(4), 202–211. https://doi.org/10.5670/oceanog.2009.109

Held, I. M., Guo, H., Adcroft, A., Dunne, J. P., Horowitz, L. W., Krasting, J., et al. (2019). Structure and performance of GFDL's CM4.0 Climate Model. *Journal of Advances in Modeling Earth Systems*, *11*(11), 3691–3727. https://doi.org/10.1029/2019ms001829

Hirt, C. W., Amsden, A. A., & Cook, J. L. (1997). An arbitrary Lagrangian-Eulerian computing method for all flow speeds. *Journal of Computational Physics*, *135*(2), 203–216. https://doi.org/10.1006/jcph.1997.5702

Huynh, H. (1995). *A piecewise-parabolic dual-mesh method for the Euler equations* (p. 1739). Paper presented at 12th Computational Fluid Dynamics Conference.

Jin, X., Gruber, N., Dunne, J. P., Sarmiento, J. L., & Armstrong, R. A. (2006). Diagnosing the contribution of phytoplankton functional groups to the production and export of particulate organic carbon, CaCO₃, and opal from global nutrient and alkalinity distributions. *Global Biogeochemical Cycles*, *20*, GB2015. https://doi.org/10.1029/2005GB002532

Jones, C. D., Arora, V., Friedlingstein, P., Bopp, L., Brovkin, V., Dunne, J., et al. (2016). C4MIP–The Coupled Climate-Carbon Cycle Model Intercomparison Project: Experimental protocol for CMIP6. *Geoscientific Model Development*, *9*(8), 2853–2880. https://doi.org/10.5194/gmd-9-2853-2016

Key, R. M., Kozyr, A., Sabine, C. L., Lee, K., Wanninkhof, R., Bullister, J. L., et al. (2004). A global ocean carbon climatology: Results from Global Data Analysis Project (GLODAP). *Global Biogeochemical Cycles*, *18*, GB4031. https://doi.org/10.1029/2004GB002247

Khatiwala, S., Tanhua, T., Mikaloff Fletcher, S., Gerber, M., Doney, S. C., Graven, H. D., et al. (2012). Global ocean storage of anthropogenic carbon. *Biogeosciences Discussions*, *9*(7), 8931–8988. https://doi.org/10.5194/bgd-9-8931-2012

Klaas, C., & Archer, D. E. (2002). Association of sinking organic matter with various types of mineral ballast in the deep sea: Implications for the rain ratio. *Global Biogeochemical Cycles*, *16*(4), 1116. https://doi.org/10.1029/2001GB001765

Kwiatkowski, L., Torres, O., Bopp, L., Aumont, O., Chamberlain, M., Christian, J. R., et al. (2020). Twenty-first century ocean warming, acidification, deoxygenation, and upper-ocean nutrient and primary production decline from CMIP6 model projections. *Biogeosciences*, *17*(13), 3439–3470. https://doi.org/10.5194/bg-17-3439-2020

Landry, M. R., Barber, R. T., Bidare, R. R., Chai, F., Coale, K. H., Dam, H. G., et al. (1997). Iron and grazing constraints on primary production in the central equatorial Pacific: An EqPac synthesis. *Limnology and Oceanography*, *42*(3), 405–418. https://doi.org/10.4319/lo.1997.42.3.0405

Landry, M. R., & Hassett, R. (1982). Estimating the grazing impact of marine micro-zooplankton. *Marine Biology*, *67*(3), 283–288. https://doi.org/10.1007/BF00397668

Laufkötter, C., John, J. G., Stock, C. A., & Dunne, J. P. (2017). Temperature and oxygen dependence of the remineralization of organic matter. *Global Biogeochemical Cycles*, *31*, 1038–1050. https://doi.org/10.1002/2017GB005643

Laufkötter, C., Vogt, M., Gruber, N., Aita-Noguchi, M., Aumont, O., Bopp, L., et al. (2015). Drivers and uncertainties of future global marine primary production in marine ecosystem models. *Biogeosciences*, *12*(23), 6955–6984. https://doi.org/10.5194/bg-12-6955-2015

Laufkötter, C., Vogt, M., Gruber, N., Aumont, O., Bopp, L., Doney, S. C., et al. (2016). Projected decreases in future marine export production: The role of the carbon flux through the upper ocean ecosystem. *Biogeosciences*, *13*(13), 4023–4047. https://doi.org/10.5194/bg-13-4023-2016

Le Quere, C. L., Harrison, S. P., Colin Prentice, I., Buitenhuis, E. T., Aumont, O., Bopp, L., et al. (2005). Ecosystem dynamics based on plankton functional types for global ocean biogeochemistry models. *Global Change Biology*, *11*(11), 2016–2040.

Liu, X., Dunne, J. P., Stock, C. A., Harrison, M. J., Adcroft, A., & Resplandy, L. (2019). Simulating water residence time in the coastal ocean: A global perspective. *Geophysical Research Letters*, *46*, 13,910–13,919. https://doi.org/10.1029/2019GL085097

Locarnini, R. A., Mishonov, A. V., Antonov, J. I., Boyer, T. P., Garcia, H. E., Baranova, O. K., et al. (2013). In S. Levitus & A. Mishonov (Eds.), *World Ocean Atlas 2013, Volume 1: Temperature, NOAA Atlas NESDIS 73* (pp. 1–40). https://doi.org/10.7289/V55X26VD

Maier-Reimer, E. (1993). Geochemical cycles in an ocean general circulation model: Preindustrial tracer distributions. *Global Biogeochemical Cycles*, *7*(3), 645–677. https://doi.org/10.1029/93GB01355

Mislan, K. A. S., Stock, C. A., Dunne, J. P., & Sarmiento, J. L. (2014). Group behavior among model bacteria influences particulate carbon remineralization depths. *Journal of Marine Research*, *72*(3), 183–218. https://doi.org/10.1357/002224014814901985

Monod, J. (1949). The growth of bacterial cultures. *Annual Reviews in Microbiology*, *3*(1), 371–394. https://doi.org/10.1146/annurev.mi.03.100149.002103

Moore, J. K., & Braucher, O. (2008). Sedimentary and mineral dust sources of dissolved iron to the world ocean. *Biogeosciences*, *5*(3), 631–656. https://doi.org/10.5194/bg-5-631-2008

Najjar, R., & Orr, J. (1998). Design of OCMIP-2 simulations of chlorofluorocarbons, the solubility pump and common biogeochemistry. In *Internal OCMIP Report*. Gif-sur-Yvette, France: LSCE/CEA Saclay.

Olsen, A., Key, R. M., Van Heuven, S., Lauvset, S. K., Velo, A., Lin, X., et al. (2016). The Global Ocean Data Analysis Project version 2 (GLODAPv2)—An internally consistent data product for the world ocean. *Earth System Science Data (Online)*, *8*(2).

O'Neill, B. C., Tebaldi, C., van Vuuren, D. P., Eyring, V., Friedlingstein, P., Hurtt, G., et al. (2016). The Scenario Model Intercomparison Project (ScenarioMIP) for CMIP6. *Geoscientific Model Development*, *9*(9), 3461–3482. https://doi.org/10.5194/gmd-9-3461-2016

Orr, J. C., & Epitalon, J. M. (2015). Improved routines to model the ocean carbonate system: MOCSY 2.0. *Geoscientific Model Development*, *8*(3), 485.

Orr, J. C., Najjar, R. G., Aumont, O., Bopp, L., Bullister, J. L., Danabasoglu, G., et al. (2017). Biogeochemical protocols and diagnostics for the CMIP6 Ocean Model Intercomparison Project (OMIP). *Geoscientific Model Development*, *10*(6), 2169–2199. https://doi.org/10.5194/gmd-10-2169-2017

Oschlies, A., Schulz, K. G., Riebesell, U., & Schmittner, A. (2008). Simulated 21st century's increase in oceanic suboxia by CO_2-enhanced biotic carbon export. *Global Biogeochemical Cycles*, *22*, GB4008. https://doi.org/10.1029/2007GB003147

Owens, T. G., Falkowski, P. G., & Whitledge, T. E. (1980). Diel periodicity in cellular chlorophyll content in marine diatoms. *Marine Biology*, *59*(2), 71–77. https://doi.org/10.1007/BF00405456

Parekh, P., Follows, M. J., & Boyle, E. A. (2005). Decoupling of iron and phosphate in the global ocean. *Global Biogeochemical Cycles*, *19*, GB2020. https://doi.org/10.1029/2004GB002280

Purkey, S. G., & Johnson, G. C. (2012). Global contraction of Antarctic bottom water between the 1980s and 2000s. *Journal of Climate*, *25*(17), 5830–5844. https://doi.org/10.1175/JCLI-D-11-00612.1

Redfield, A. C., Ketchum, B. H., & Richards, F. A. (1963). The influence of organisms on the composition of the sea water. In M. N. Hill (Ed.), *The sea* (Vol. 2, pp. 26–77). New York: Interscience Publishers.

Séférian, R., Berthet, S., Yool, A., Palmiéri, J., Bopp, L., Tagliabue, A., et al. (2020). Tracking improvement in simulated marine biogeochemistry between CMIP5 and CMIP6. *Current Climate Change Reports*. https://doi.org/10.1007/s40641-020-00160-0

Séférian, R., Gehlen, M., Bopp, L., Resplandy, L., Orr, J. C., Marti, O., et al. (2016). Inconsistent strategies to spin up models in CMIP5: Implications for ocean biogeochemical model performance assessment. *Geoscientific Model Development*, *9*(5), 1827–1851. https://doi.org/10.5194/gmd-9-1827-2016

Stock, C., & Dunne, J. (2010). Controls on the ratio of mesozooplankton production to primary production in marine ecosystems. *Deep Sea Research Part I: Oceanographic Research Papers*, *57*(1), 95–112. https://doi.org/10.1016/j.dsr.2009.10.006

Stock, C. A., Dunne, J. P., Fan, S., Ginoux, P., John, J., Krasting, J., et al. (2014a). Global-scale carbon and energy flows through the marine planktonic food web: An analysis with a coupled physical-biological model. *Progress in Oceanography*, *120*, 1–28. https://doi.org/10.1016/j.pocean.2013.07.001

Stock, C. A., Dunne, J. P., & John, J. G. (2014b). Drivers of trophic amplification of ocean productivity trends in a changing climate. *Biogeosciences*, *11*(24), 7125–7135. https://doi.org/10.5194/bg-11-7125-2014

Stock, C. A., Dunne, J. P., Fan, S., Ginoux, P., John, J., Krasting, J., et al. (2020). Ocean Biogeochemistry in GFDL's Earth System Model 4.1 and its Response to Increasing Atmospheric CO_2. *Journal of Advances in Modeling Earth Systems*, *12*, e2019MS002043. https://doi.org/10.1029/2019MS002043

Strzepek, R. F., & Harrison, P. J. (2004). Photosynthetic architecture differs in coastal and oceanic diatoms. *Nature*, *431*(7009), 689–692. https://doi.org/10.1038/nature02954

Sunda, W. G., & Huntsman, S. A. (1997). Interrelated influence of iron, light and cell size on marine phytoplankton growth. *Nature*, *390*(6658), 389–392. https://doi.org/10.1038/37093

Tagliabue, A., Aumont, O., DeAth, R., Dunne, J. P., Dutkiewicz, S., Galbraith, E., et al. (2016). How well do global ocean biogeochemistry models simulate dissolved iron distributions? *Global Biogeochemical Cycles*, *30*, 149–174. https://doi.org/10.1002/2015GB005289

Thiele, G., & Sarmiento, J. L. (1990). Tracer dating and ocean ventilation. *Journal of Geophysical Research*, *95*(C6), 9377–9391. https://doi.org/10.1029/JC095iC06p09377

Toggweiler, J. R. (1999). Oceanography: An ultimate limiting nutrient. *Nature*, *400*(6744), 511–512. https://doi.org/10.1038/22892

Tyrrell, T. (1999). The relative influences of nitrogen and phosphorus on oceanic primary production. *Nature*, *400*(6744), 525–531. https://doi.org/10.1038/22941

Wallmann, K. (2010). Phosphorus imbalance in the global ocean? *Global Biogeochemical Cycles*, *24*. https://doi.org/10.1029/2009GB003643

Zhao, M., Golaz, J.-C., Held, I. M., Guo, H., Balaji, V., Benson, R., et al. (2018). The GFDL global atmosphere and land model AM4.0/LM4.0: 2. Model description, sensitivity studies, and tuning strategies. *Journal of Advances in Modeling Earth Systems*, *10*(3), 735–769. https://doi.org/10.1002/2017MS001209

Zweng, M. M., Reagan, J. R., Antonov, J. I., Locarnini, R. A., Mishonov, A. V., Boyer, T. P., et al. (2013). *World Ocean Atlas 2013, Volume 2: Salinity*. In S. Levitus & A. Mishonov (Eds.), *NOAA Atlas NESDIS 74* (pp. 1–39).